Marine and Petroleum Geology 154 (2023) 106302

Contents lists available at ScienceDirect

Marine and Petroleum Geology

journal homepage: www.elsevier.com/locate/marpetgeo

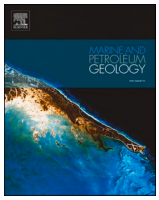

Oil occurrence state and quantity in alkaline lacustrine shale using a high-frequency NMR technique

Chenxi Zhang [a,b], Fujie Jiang [a,b,*], Tao Hu [a,b], Di Chen [a,b], Liliang Huang [c], Zhenxue Jiang [a,d], Xiaohao Wang [a,b], Zheyu Liu [a,b], Yuping Wu [a,b], Jiahao Lv [a,b], Renda Huang [a,b], Meiling Hu [a,b], Guanyun Wu [a,b]

[a] State Key Laboratory of Petroleum Resources and Prospecting, China University of Petroleum, Beijing, 102249, China
[b] College of Geosciences, China University of Petroleum (Beijing), Beijing, 102249, China
[c] Research Institute of Petroleum Exploration and Development, Xinjiang Oilfield Company, CNPC, Karamay, Xinjiang, 834000, China
[d] The Unconventional Oil and Gas Institute, China University of Petroleum, Beijing, 102249, China

ARTICLE INFO

Keywords:
NMR
Fengcheng Fm shale
Lithofacies
Occurrence state
Movability

ABSTRACT

Complex fluid occurrence states and structures of shale reservoirs greatly affect shale oil productivity. For lacustrine shales with strong heterogeneity, it is important to identify oil movability, occurrence states and pore structures in different lithofacies in order to efficiently develop shale oil. This study combines conventional core analysis, X-ray diffraction (XRD), argon ion milled-scanning electron microscopy (AIM-SEM), multiple isothermal stages (MIS) pyrolysis and high-frequency nuclear magnetic resonance (HF-NMR) to create maps for samples in native, saturated, centrifuged, and dried states. A new T_1-T_2 map interpretation scheme is proposed, and fluid occurrence models for different shale lithofacies are established. Four oil species can be identified on the T_1-T_2 map. Free oil and adsorbed oil in macropores are located in the centers and edges of intergranular/intercrystalline pores, respectively. Oil in mesopores is located in intragranular/intracrystalline dissolution pores. Adsorbed oil exists in the pores of dispersed organic matter and in the marginal fractures of organic matter laminae. NMR and pyrolysis correlate well in the oil contents that they define. The occurrence state of shale oil in the Fengcheng Fm is closely related to minerals and organic matter. Siliceous minerals are beneficial to the occurrence of free oil that is usually a highly movable. The fluid-holding capacity of calcareous shale is limited, especially for adsorbed oil and restricted oil. Clay minerals (>10%) are not conducive to shale oil enrichment and flow, and mixed shale almost exclusively contains bound water. Organic matter is conducive to increasing oil content and to the movable oil saturation of siliceous shale and mixed shale.

1. Introduction

As a key part of unconventional resources, shale oil shows huge resource potential and has received great attention worldwide. The breakthroughs of shale oil in the Bakken and Eagle Ford shales show the broad resource prospects of shale oil resources (Curtis, 2002; Jarvie et al., 2007; Sonnenberg and Pramudito, 2009; Hui and Sonnenberg, 2013; Jin et al., 2017). Horizontal drilling combined with hydraulic fracturing has been developed for shale formations to increase oil recovery by nearly 10%, with recovery in the Bakken formation reaching up to 19% (Clark, 2009; Davis, 2018; Altawati et al., 2021; Lei et al., 2021). However, most shale reservoirs retain significant amounts of oil after the initial exploitation is completed, and overall oil recovery remains low. Shale reservoirs have the characteristics of strong heterogeneity in biological populations, mineral composition and structure (Katz, 1990); ultralow porosity (<10%) and permeability (<0.1 mD) (Liu et al., 2020); abundant clay and organic matter (Katz, 1990; Nelson, 2009; Jarvie, 2012a, b; Katz and Fang, 2014), showing complex geological characteristics. In addition, compared with light marine shale oil, lacustrine shale oil is more viscous (Wang et al., 2019) and therefore less movable, especially in China (Zou et al., 2019).

Movability is a key parameter in shale oil evaluation and is mainly affected by the occurrence state of crude oil and the pore structure of shale. Crude oil generally exists in the status of free, adsorbed and dissolved in shale reservoirs (; Jarvie, 2012a, b; Sang et al., 2018). “Free oil” exists in large pores and fractures (O’Brien et al., 2002); “adsorbed

* Corresponding author. State Key Laboratory of Petroleum Resources and Prospecting, China University of Petroleum, Beijing, 102249, China.
E-mail address: jfjhtb@163.com (F. Jiang).

https://doi.org/10.1016/j.marpetgeo.2023.106302
Received 16 February 2023; Received in revised form 22 April 2023; Accepted 26 April 2023
Available online 2 May 2023

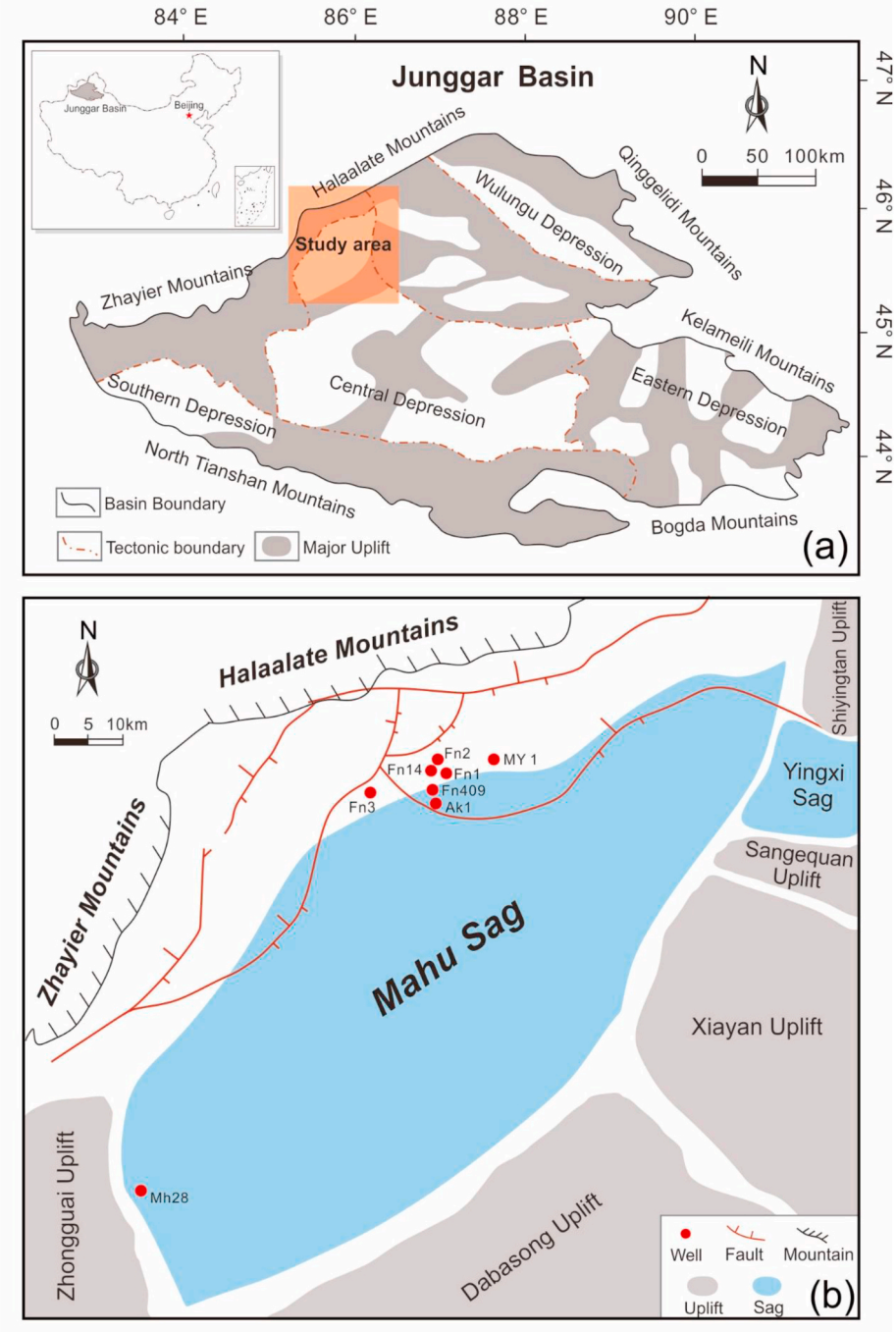

Fig. 1. Location map of study area. (a) Schematic map of the Junggar Basin and its location in China (modified after Wang et al. (2021)). (b) Tectonic setting map of the Mahu sag showing the uplifts, sags, faults and locations of shale oil wells, where the studied samples were obtained (modified after Wang et al. (2021)).

oil" is attached to the surface of organic matter and mineral pores under the action of van der Waals forces and Coulomb forces (Curtis, 2002); "dissolved oil" is located in the space supported by the kerogen skeleton (Van Heek, 2000). Their composition, density and viscosity are different (Zhu et al., 2021), and the movability of these oil types decreases from free oil to dissolved oil. At present, only free oil is the resource that can be exploited preferentially (Jarvie, 2012a, b; Larter et al., 2012).

There are many evaluation methods for the movable oil in shale, including the multiple isothermal stages (MIS) pyrolysis program (Jiang et al., 2016a, b; Romero-Sarmiento et al., 2016), multistep solvent extraction method (Qian et al., 2017), kerogen swelling method (Li et al., 2016a), nuclear magnetic resonance (NMR) (Dunn et al., 2002) and molecular dynamics simulation (Wang et al., 2015). Among them, MIS and NMR experiments are convenient and fast and can more completely characterize fluids with different occurrence states and quantitatively evaluate movable oil (Jiang et al., 2016a, b; Khatibi et al., 2019; Zhang et al., 2020). MIS pyrolysis is based on the principle that shale oil with different occurrence states will be released in an orderly manner with increasing temperature (Hu et al., 2021), and the release process is restricted by the size, connectivity and wettability of pores (Zhang et al., 2020). By adjusting the pyrolysis temperature procedure, four key parameters are obtained: $S_{1\text{-}1}$, $S_{1\text{-}2}$, $S_{2\text{-}1}$ and $S_{2\text{-}2}$, which are light oil (C_5–C_{12}), light-medium oil (C_{12}–C_{22}), heavy oil-solid bitumen (C_{22}–C_{40}) and pyrolysis hydrocarbon from kerogen, respectively. Additionally, ($S_{1\text{-}1}$+$S_{1\text{-}2}$) and ($S_{1\text{-}1}$+$S_{1\text{-}2}$+$S_{2\text{-}1}$) are the maximum movable oil content and total oil content, respectively (Jiang et al., 2016a, b).

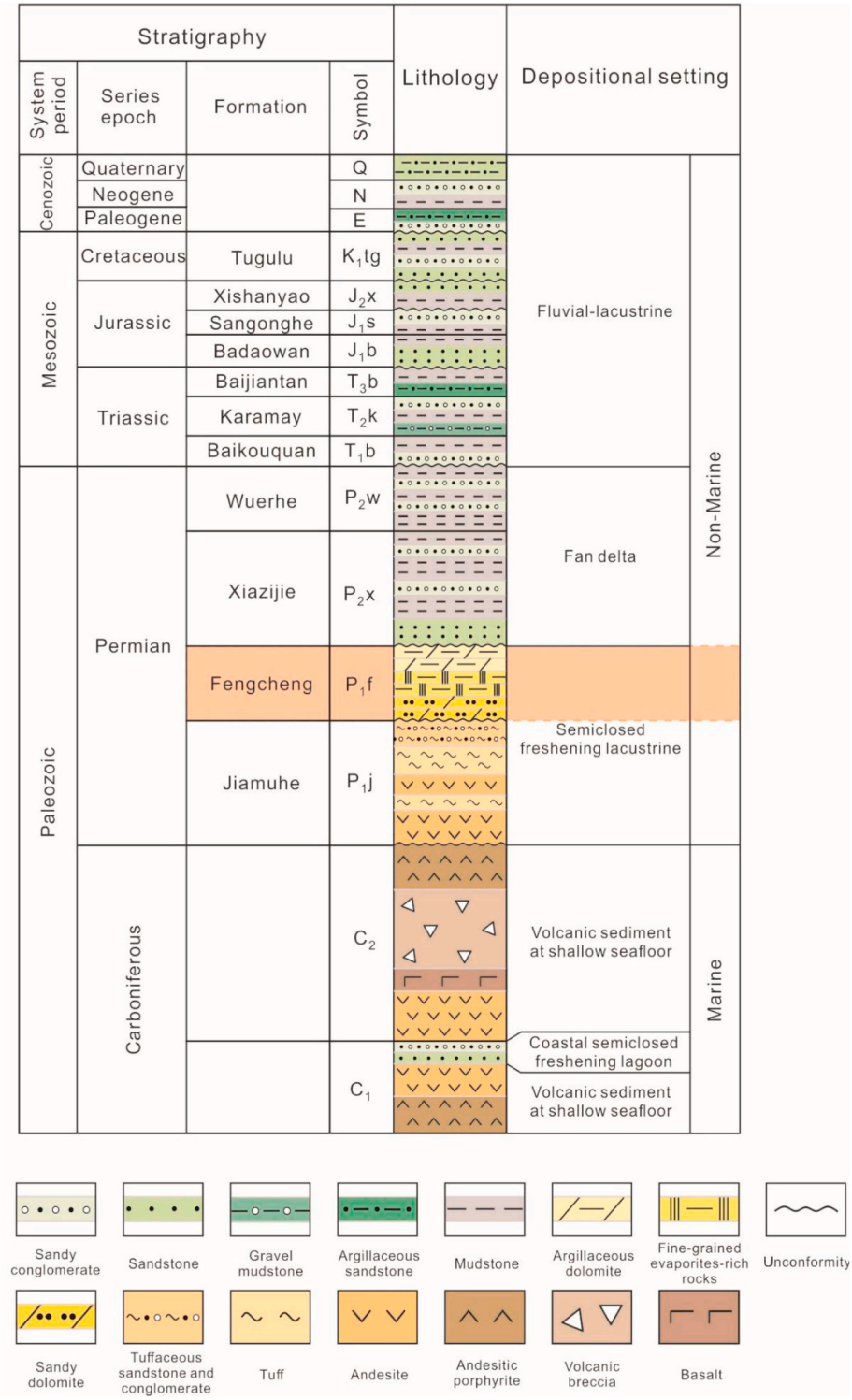

Fig. 2. Detailed geological column of the Mahu Sag (modified after Yu et al. (2019).The Fengcheng Formation is located in the lower Permian and is highlighted in orange.

However, methods such as MIS pyrolysis may damage the quality of the sample to a certain extent because the comminution process destroys part of the pores and affects the estimated content of total oil and movable oil. In contrast, NMR is a noninvasive and nondestructive measurement technique. It preserves sample integrity and reduces the effects of heterogeneity (Birdwell and Washburn, 2015; Kausik et al., 2016).

However, commonly used low-frequency (2 MHz) NMR is not sensitive to the response of hydrogen-containing fluids in shale, resulting in low resolution for oil and water, such as the mixed crossover of bitumen and irreducible water signals (Washburn and Birdwell, 2013; Kausik et al., 2016). Since the T_1/T_2 of the oil signal increases with frequency, high-frequency NMR (higher than 20 MHz) has a higher sensitivity and shorter echo interval than low-frequency NMR (Nicot et al., 2016). High-frequency NMR (HF-NMR) is more effective at separating different proton groups and quickly gained attention and

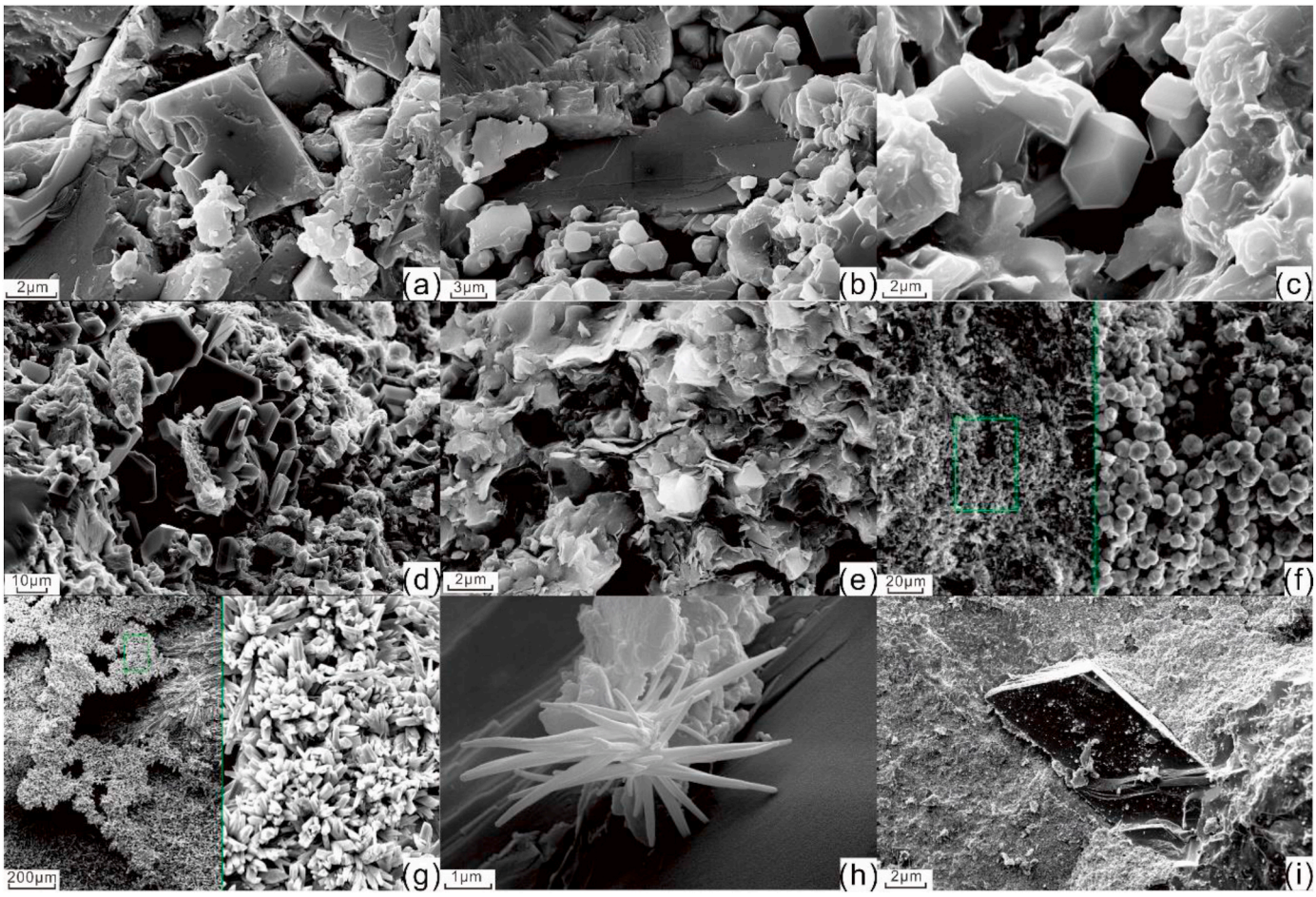

Fig. 3. Microscopic characteristics of main minerals in the Fengcheng Formation shale. (a) Dolomite crystal, MY1, 4595.6m; (b) calcite crystal, MY1, 4669.6m; (c) quartz grain, MY1, 4612.3m; (d) tabular albite crystal, MY1, 4612.3m; (e) flake illite in matrix, MY1, 4700.7m; (f) pyrite aggregate and partial amplification, FC1, 4274.61m; (g) short columnar gypsum crystals and partial magnification, FN7, 4591m; (h) reedmergnerite crystal, FN7, 4590m; (i) granular columnarzeolites, MH28, 4180.1m.

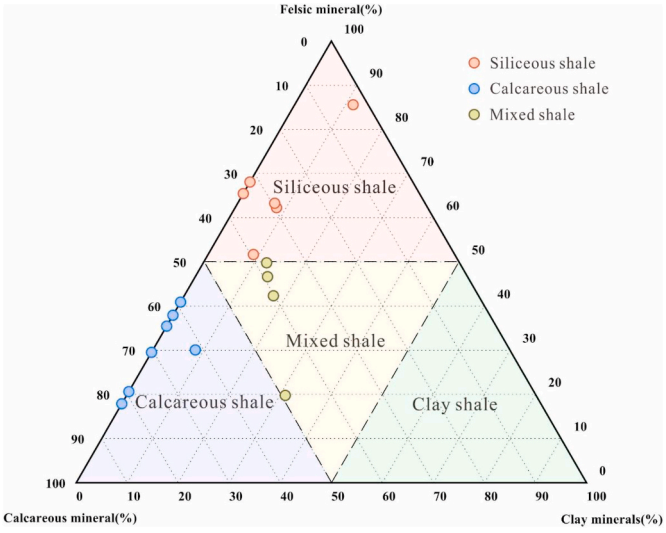

Fig. 4. Mineral composition of siliceous shale, calcareous shale and mixed shale of the Fengcheng Formation.

acceptance in unconventional core analysis (Korb et al., 2014; Khatibi et al., 2019; Gentzis et al., 2021).

Previous studies have used HF-NMR to finely characterize the occurrence state of shale oil and established a fluid division chart based on the T_1-T_2 map, which is of great significance for the evaluation of shale oil movability (Singer, 2013; Birdwell and Washburn, 2015; Fleury and Romero-Sarmiento, 2016; Nicot et al., 2016; Li et al., 2020a; Mukhametdinova et al., 2021; Zhang et al., 2022). For example, Fleury and Romero-Sarmiento used two-dimensional distribution NMR data at 23.7 MHz to provide a qualitative interpretation of the oil occurrence state in the Mississippian Barnett Shale, Fort Worth Basin (Fleury and Romero-Sarmiento, 2016). Nicot et al. continued Fleury's T_1-T_2 interpretation scheme and calculated the oil saturation of source rock samples from the Vaca Muerta Formation in Argentina using a T_1-T_2 map. Li et al. tested the T_1-T_2 maps of the Shahejie Formation shale of the Damintun Sag, Bohai Bay Basin, under different oil and water conditions and identified a variety of hydrogen-containing components (kerogen, free oil, adsorbed oil, free water, adsorbed water, etc.) (Li et al., 2018). Khatibi synthesized previously published papers on T_1-T_2 interpretation schemes and produced universal T_1-T_2 maps (Khatibi et al., 2019). However, there are obvious differences between the T_1-T_2 fluid classification standards established by scholars, and the applicability of maps is still uncertain. For strongly heterogeneous lacustrine shales, these uncertainties may lead to misestimates of the movable oil amount. In addition, lithofacies is an important factor affecting the occurrence state and content of shale oil (Wang et al., 2019). Therefore, it is very important to establish an applicable T_1-T_2 interpretation scheme and discuss it based on lithofacies classification.

Large lacustrine shale oil resources have been found in the organic-

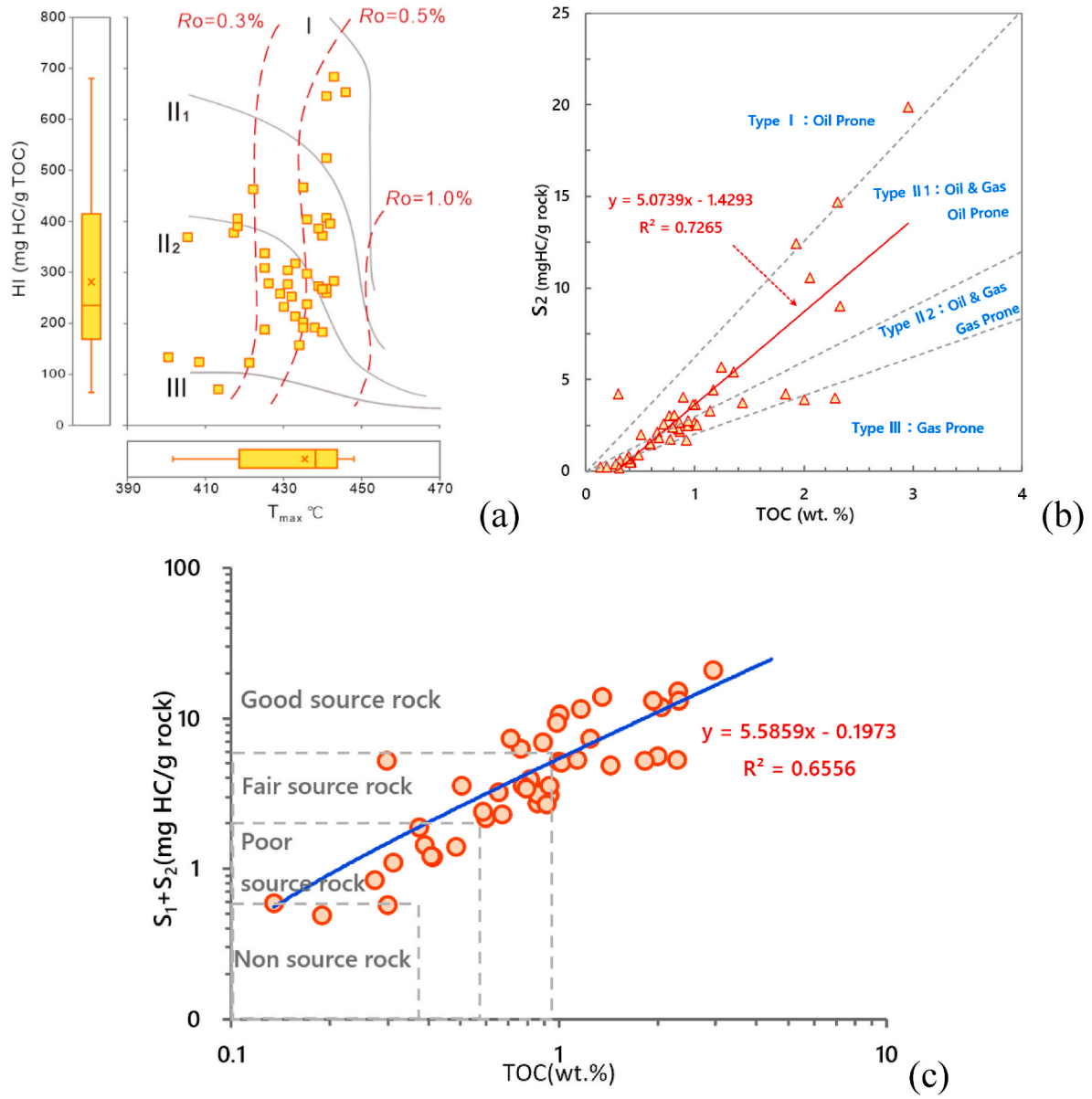

Fig. 5. Geochemical characteristics of the Fengcheng Formation shale. (a) Hydrogen index (HI) versus Tmax plot showing the kerogen type and maturity. (b) S_2 versus TOC plot showing the quantity and quality of organic matter, kerogen type (modified after Wang et al. (2015)). (c) S_1+S_2 versus TOC plot showing organic matter abundance and hydrocarbon production capacity.

rich shale of the Permian Fengcheng Fm in the Mahu Sag, Junggar Basin, NW China. Fengcheng Fm shales are highly heterogeneous, with significant differences in organic matter abundance and mineral composition, which are suitable for the study of differences in fluid occurrence state and movability in different lithofacies. Therefore, high-frequency (21.36 MHz) NMR relaxation measurements are taken for shale samples from the Fengcheng Fm with different oil saturations, and T_1-T_2 fluid classification maps suitable for alkaline lake shale are proposed in this study. Combined with NMR, AIM-SEM, routine pyrolysis and MIS pyrolysis, fluid occurrence patterns are compared, and the amount of movable oil is quantitatively evaluated in different lithofacies. This work reveals the mechanism of the influence of minerals, organic matter and pore structure on the fluid of different occurrence states in shale. It is helpful to accurately identify high-movability stratigraphy and to provide theoretical guidance for the efficient exploration and development of shale oil.

2. Geological setting

The Junggar Basin is in northwestern China and has an area of approximately 13.6×10^4 km^2 (Zheng et al., 2019). The Junggar Basin is located in the western Kelameili orogenic belt and the northern Tianshan orogenic belt (Fig. 1a). According to the evolution process and characteristics of the basin, the Junggar Basin can be divided into six first-order tectonic units with significant differences in structural morphology and styles (Li et al., 2021). The Mahu Sag is an oil-rich foreland sag located in the western Junggar Basin, with an area of 5000 km^2 (Fig. 1b) (Wang et al., 2021). The Mahu Sag is located in the northwest of the central depression and belongs to a secondary negative tectonic unit. The overall distribution is from northeast to southwest, with a rugby ball shape that is narrow in the north and slightly wider in the south. The western and northern sides of the Mahu Sag are confined by the Wuxia-Kebai fault zone, which is most important in the northwestern margin of the Junggar Basin, and the eastern and southern sides are adjacent to the Yingxi Sag, Xiayan Uplift, Dabasong Uplift and

Table 1
Standard Rock-Eval pyrolysis, TOC, depth and mineral composition data of shale samples.

Well	Sample ID	Depth (m)	TOC (wt.%)	S_1 (mg/g rock)	S_2 (mg/g rock)	HI (mg/g TOC)	T_{max} (°C)	OT	Quartz (wt.%)	Feldspar (wt.%)	Calcite (wt.%)	Dolomite (wt.%)	Clay (wt.%)	Pyrite (wt.%)
FN1	J-5	4321.0	0.65	1.09	2.15	329	426	II_2	22.4	23.6	13.9	21.2	7.9	5.1
MY1	BJ-14	4708.9	0.77	3.21	3.03	395	437	II_2	51.3	13.8	3.8	26.7	0.0	4.4
MY1	BJ-20	4812.6	0.85	0.97	2.33	275	444	II_2	51.8	10.4	14.0	18.8	0.0	4.9
MY1	BJ-21	4807.9	0.86	0.57	2.16	251	442	II_2	28.4	26.2	8.9	17.0	7.4	8.7
MY1	BJ-8	4911.8	1.00	6.91	3.65	364	441	I	17.8	34.6	3.1	21.3	6.0	3.0
MY1	BJ-4	4910.6	1.36	8.39	5.40	398	442	II_2	47.0	24.2	2.6	0.0	9.4	0.0
FN-409	J-9	4528.0	0.31	0.53	0.56	180	426	II_2	2.9	16.1	31.5	41.6	0.0	4.4
AK-1	J-28	5667.8	0.41	0.67	0.52	126	401	II_2	0.0	12.5	45.0	12.4	0.0	17.5
FN1	J-7	4362.9	0.81	0.83	3.07	378	440	II_2	10.8	21.5	42.2	10.7	0.0	7.6
MY1	BJ-12	4711.0	0.94	0.60	2.48	265	440	II_2	17.2	14.7	28.0	30.1	0.0	4.5
MY1	BJ-13	4694.3	1.43	1.15	3.72	260	442	II_2	11.7	15.4	33.1	31.6	0.0	8.2
MY1	BJ-1	4594.6	2.33	4.03	9.01	387	443	I	9.6	18.6	28.9	28.9	7.8	6.2
FN2	J-13	4041.8	2.95	0.91	19.90	674	444	II_2	26.7	10.9	24.7	29.6	0.0	8.0
FN14	J-15	4033.1	0.14	0.35	0.24	178	372	III	17.4	2.4	14.2	35.0	31.1	0.0
MH28	J-22	4843.3	0.27	0.43	0.41	149	435	III	27.6	21.6	8.8	13.7	11.4	5.3
FN3	J-12	3955.6	1.02	2.48	2.55	250	430	III	0.7	39.2	13.0	20.5	12.1	0.0
MY1	BJ-18	4772.0	1.93	0.57	12.43	644	447	III	11.2	24.2	3.0	30.6	14.6	8.4

TOC = total organic carbon, HI = hydrocarbon index, Tmax = maximum temperature of S_2, OT = Organic type.

Zhongguai Uplift (Lei et al., 2017).

The lower Permian Fengcheng Fm is the main source rock strata and reservoir in this area (Fig. 2). It contains alternating deposits of volcanic material, terrigenous clasts and endogenous carbonate grains (Zhang et al., 2018), forming a unique sequence of fine-grained sedimentary rocks deposited in an alkaline lake (Li et al., 2021). From bottom to top, the Fengcheng Fm is divided into Mbr 1, Mbr 2 and Mbr 3. Mbr 1 of the Fengcheng Fm is dominated by siliceous shale and dolomitic shale, and volcanic rocks are present at the bottom. Mbr 2 of the Fengcheng Fm is mainly composed of dolomitic shale and argillaceous siltstone, and a large amount of alkaline evaporative rock formation is present in the center of deposition. Interbedded dolomitic shale, argillaceous dolomite and siliceous shale of unequal thickness are present at the bottom of Mbr 3 of the Fengcheng Fm (Cao et al., 2020; Zhi et al., 2021).

3. Methodology

3.1. Sample

Seventeen samples were collected from the Fengcheng Fm in Well MY1, where industrial oil flows have been obtained, and 7 other wells around Well MY1 in the Mahu Sag (Fig. 1b). They were prepared as powders, fragments and cores for pyrolysis, AIM-SEM and NMR tests, respectively.

3.2. Methods

3.2.1. TOC and XRD

TOC was determined by a CS-230HC carbon sulfur analytical instrument. First, the core was crushed to 80–100 mesh, placed in a crucible, dripped with dilute HCl, and heated in a water bath for 48 h until carbonate minerals fully reacted. Then the sample was cleaned with distilled water. After drying for 12 h, iron and tungsten were added to the crucible as accelerants and burned in high-temperature oxygen flow to obtain experimental results. The other sample was crushed to approximately 300 mesh. The powder was pressed into the container by the back pressure method, keeping the upper surface even and placed in a Brucker D8 Focus instrument for XRD analysis.

3.2.2. Routine pyrolysis and MIS pyrolysis

Each sample was washed and ground to 100 mesh and then divided into two identical portions. One was put into the pyrolysis furnace of a Rock-Eval VI device for conventional rock pyrolysis (State Key Laboratory of Oil and Gas Resources and Exploration, China). The temperature was maintained at 300 °C for 3 min to obtain S_1, and then the temperature was increased to 650 °C at a rate of 50 °C/min to obtain S_2 and Tmax. Another sample was tested using MIS pyrolysis proposed by Jiang et al. (2016b)(Sinopec Petroleum Exploration and Production Research Institute, China). The sample was carried out with the following procedure: The initial temperature was set to 80 °C, then increased to 200 °C and held for 1 min to obtain $S_{1\text{-}1}$. Then, the temperature was increased to 350 °C and maintained for 1 min to obtain $S_{1\text{-}2}$. Next, the temperature was increased from 350 °C to 450 °C and maintained at 450 °C for 1 min to obtain $S_{2\text{-}1}$. Finally, the sample was heated to 600 °C and held for 1 min to obtain $S_{2\text{-}2}$. They are directly detected by a flame ionization detector.

3.2.3. AIM-SEM

The samples were cut into 1 cm^3 irregular cubes. The observation surface was polished by argon (Ar) ions (Reed and Loucks, 2007; Loucks et al., 2009). A Zeiss CrossBeam 540 field emission scanning electron microscope was used to observe the microscopic morphology and structure of the samples. Backscattered electrons were imaged at an accelerating voltage of 8 kV.

3.2.4. HF-NMR relaxometry

3.2.4.1. Principle of NMR spectrometry. NMR measurement is achieved by controlling the magnetic moment of the hydrogen atomic nucleus in the presence of pulsed and static magnetic fields. NMR relaxation times can be decomposed into longitudinal relaxation time (T_1) and transverse relaxation time (T_2). T_1 is the characteristic time for the system to return to equilibrium measurements, which usually takes more time. T_2 is the characteristic time to process the loss of coherence of the secondary magnetic field. T_2 is preferred in laboratory measurements because it can be measured faster and reflects the same pore size distribution and fluid information as T_1 (Kleinberg et al., 1993; Yao et al., 2010).

For shale saturated in a wetting phase fluid, the NMR T_2 spectral signal amplitude is proportional to the number of hydrogen nuclei, so it can reflect the fluid-filled pore volume and pore size distribution (Lewis et al., 2013; Li et al., 2015; Piedrahita and Aguilera, 2017). T_2 is controlled by three different relaxation mechanisms in rocks: bulk relaxation, surface relaxation and diffusion relaxation (Livo et al., 2020; Ge et al., 2021). The integrated T_2 is expressed as:

$$1/T_2 = 1/T_{2b} + 1/T_{2s} + 1/T_{2d} \quad (1)$$

Bulk relaxation time (T_{2b}) occurs in the fluid away from the pore surface. The surface relaxation time (T_{2s}) is produced by the interaction

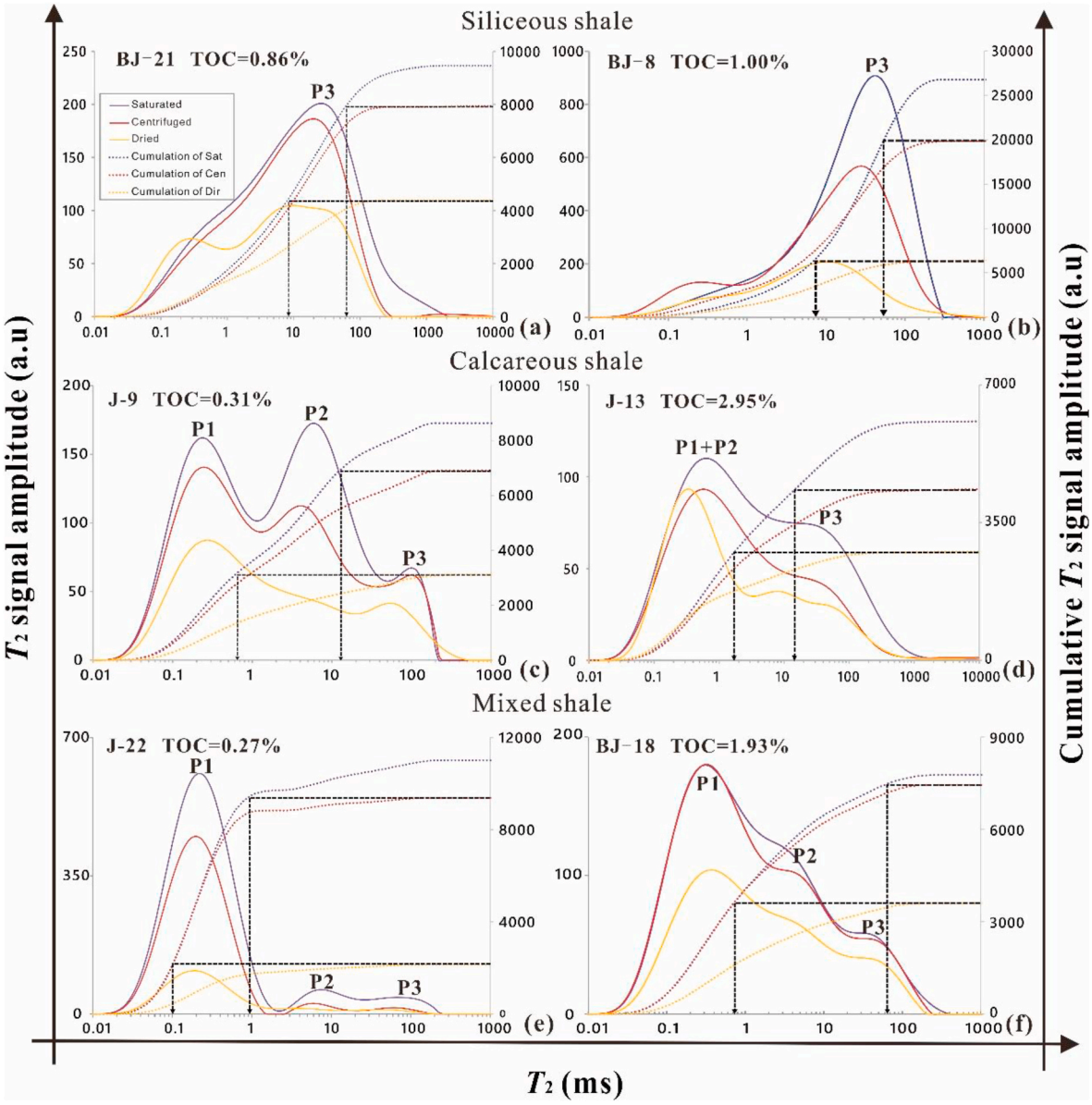

Fig. 6. T_2 spectra of shale samples in different states. The curves of solid purple (dotted purple) represent the incremental (cumulative) T_2 spectra at 100% saturation; the curves of solid red (dotted red) represent the incremental (cumulative) T_2 spectra after centrifuging; the curves of solid yellow (dotted yellow) represent the incremental (cumulative) T_2 spectra after extraction and heat treatment.

Table 2
The pore volume ratios of different pore diameters in different lithofacies in the Fengcheng Formation shale. Pore diameters were obtained by T_2 spectrum conversion, and the pore diameter classification was based on Rouquerol et al. (1994).

Lithofacies	Pore diameter distribution (%)		
	Micropore (<2 nm)	Mesopore (2–50 nm)	Macropore (>50 nm)
Siliceous shale	1.88	31.69	66.43
Calcareous shale	8.44	58.01	33.55
Mixed shale	18.51	66.68	14.81

of molecules at the contact interface between the fluid and pore surface and is closely related to the surface properties and volume of the pore. The diffusion relaxation time (T_{2d}) results from the particle spin diffusion motion of hydrogen nuclei in fluids (Lewis et al., 2013).

The bulk relaxation time is usually ignored in the nanoscale pores of shale because it is several seconds long, much longer than the surface relaxation time. In addition, the diffusive relaxation time is negligible under the conditions of a stable magnetic field and short echo interval (Daigle et al., 2014). Therefore, T_2 is mainly controlled by surface relaxation under our experimental conditions and has the following relationship with pore structure parameters:

$$1/T_2 \approx 1/T_{2s} = \rho_2 \times S/V = \rho_2 \times Fs/d \quad (2)$$

where.

ρ_2 is the surface relaxivity (μm/s) (Daigle et al., 2014). S refers to the internal surface area of the rock skeleton (μm^2). V represents the effective pore volume (μm^3). S/V is the specific surface area of the pores (1/μm). d denotes the pore diameter (μm). Fs is the dimensionless pore shape factor (Müller-Huber et al., 2016).

According to Eq. (2), the T_2 distribution of shale samples can approximate the pore size distribution, and a longer T_2 corresponds to a pore with a larger size (Kleinberg et al., 1993; Coates et al., 2007). On

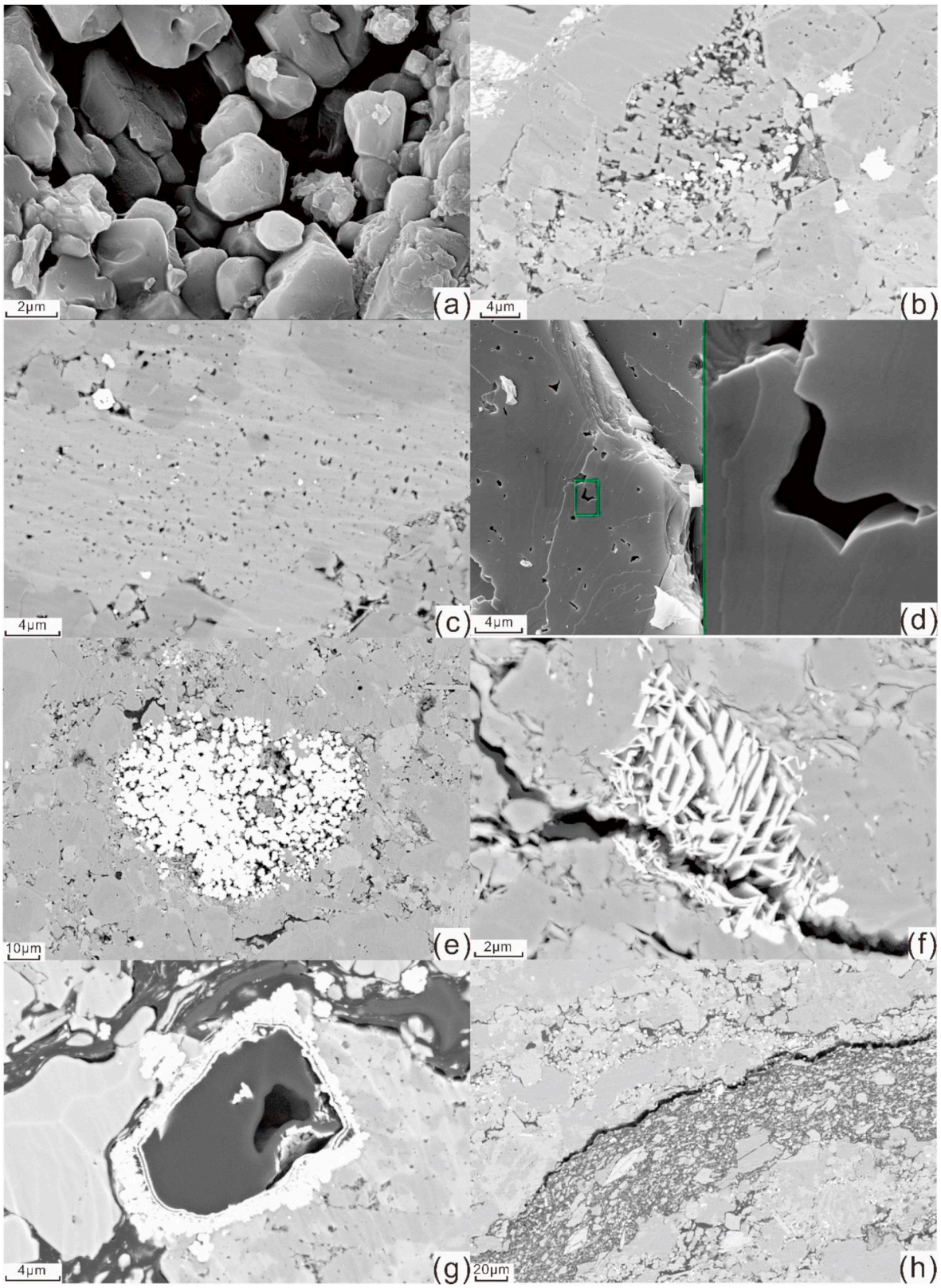

Fig. 7. SEM images of the pore system of the Fengcheng Formation shale. (a) Intergranular pores between quartz particles, MY1, 4633.8m; (b) intercrystalline pores between calcite crystals, MY1, 4594.6m; (c) intragranular dissolution pores in feldspar, MY1, 4744.9m; (d) intracrystalline dissolution pores in calcite crystal, MY1, 4669.6m; (e) intercrystalline pores in pyrite, FN3, 4147.5m; (f) parallel intragranular pores between clay minerals, FN14, 4082m; (g) organic matter pores, FN1, 4340m; (h) organic matter microfractures, FN1, 4340m.

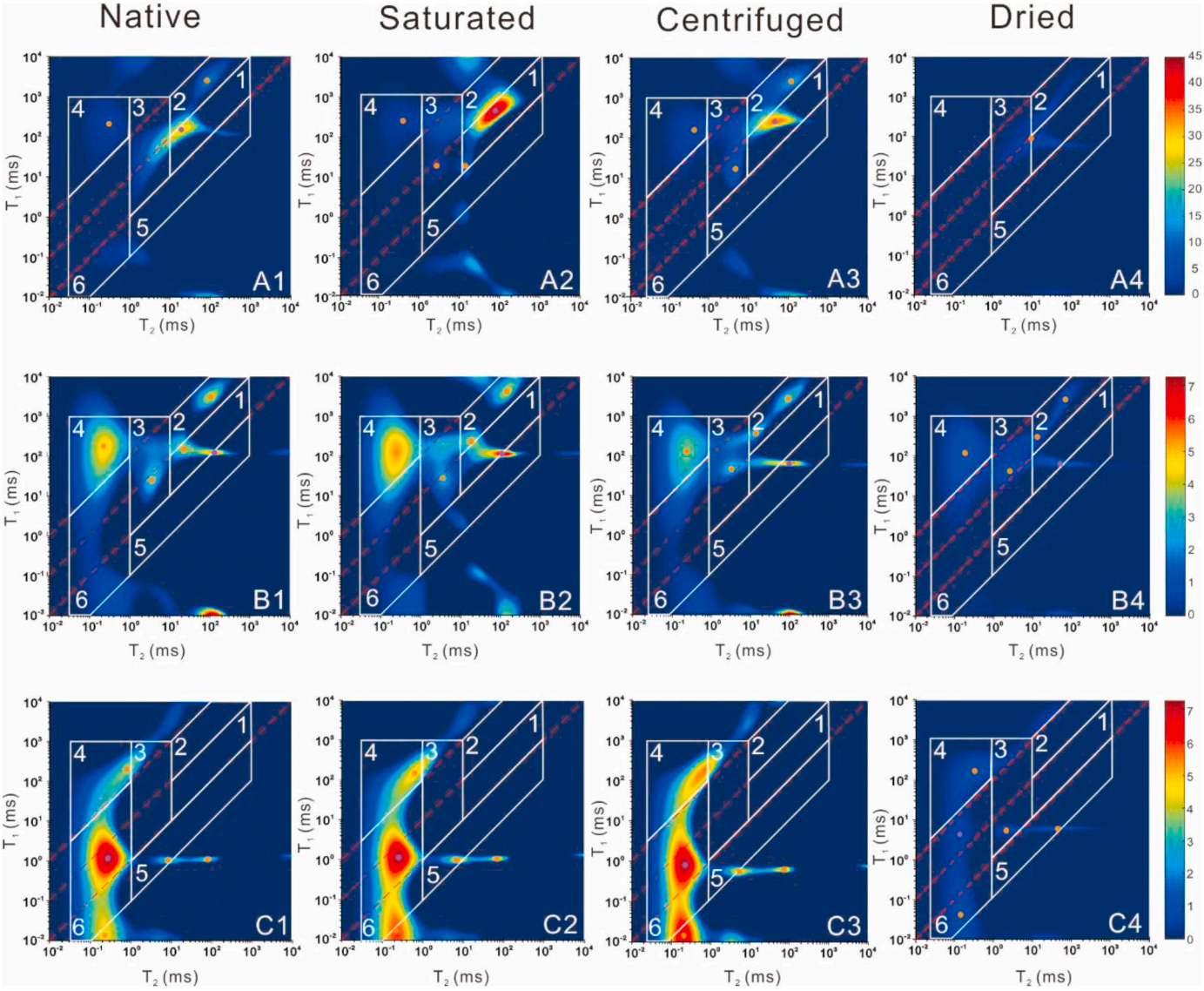

Fig. 8. T_1-T_2 maps for the target rock samples in different saturation states. Lithofacies are represented by letters: A-siliceous shale (Sample ID: BJ-8); B-calcareous shale (Sample ID: J-13); C-mixed shale (Sample ID: J-22). Oil saturation is expressed numerically: 1-native state; 2-saturation state; 3-centrifugation state; 4-dryness state. The same color bar is used in each kind of lithofacies for easy of comparison.

this basis, the cutoff value of movable fluid can be obtained in combination with centrifugation experiments.

In the T_1-T_2 map, signals of different types of hydrogen proton groups (water, oil, and solid organic matter) can be unambiguously assigned to the T_1-T_2 map by choosing appropriate T_2 and T_1/T_2 values (Korb et al., 2014; Nicot et al., 2016; Li et al., 2018; Khatibi et al., 2019; Gentzis et al., 2021). The T_1/T_2 value of hydrocarbons is more sensitive to frequency than that of water and thus can be used to easily separate them (T_1/T_{2oil} of ~10 and T_1/T_{2water} of ~1.36) (Korb et al., 2014). According to the Bloembergen–Purcell–Pound (BPP) relaxation model (Bloembergen et al., 1948), as T_2 becomes shorter and T_1/T_2 increases, the molecular mobility of fluids decreases, representing a reduction in the space to hold fluid or fluid viscosity increases (Kleinberg et al., 1993; Gentzis et al., 2021). However, when light oil molecules are located in organic pores, their T_1/T_2 value will be higher (Nicot et al., 2016).

3.2.4.2. Experimental procedure. HF-NMR measurements were performed using a MesoMR23-060H–I instrument which has a constant magnetic field strength and temperature were 0.5 T and 32 °C, respectively. The resonance frequency was 21.36 MHz. T_2 was measured using a Carr–Purcell–Meibo–Gill (CPMG) pulse sequence (Carr and Purcell, 1954; Meiboom, 1958). T_1-T_2 tests were performed by using the same pulse sequence but with 24 log-spaced inversion recovery steps and inversion using the fast inverse Laplace transform (Kausik et al., 2016). The test parameters were as follows: time of echo (TE), 0.1 ms; number of scans (NS), 64; waiting time (WT), 2,000 ms; number of echoes (NE), 10,000; and number of inversion times, 61.

Samples of different lithofacies were selected for multiple NMR tests according to the following steps: 1) Samples were first measured at as-received state (native state); 2) saturated with kerosene for 48 h at 35 MPa under vacuum conditions (saturation state); 3) centrifuged at 12,000 r/min for 8 h (centrifugation state); 4) extracted with a methanol/dichloromethane (1/9 vol) solution for 20 days and then dried (dryness state). The reasons for choosing kerosene instead of water are as follows: 1) Abundant clay particles in shale may undergo obvious hydration expansion when they encounter water, which may block the pores (Díaz-Pérez et al., 2007; Anderson et al., 2010). 2) The wettability of the pore surface of organic shale is dominated by oil wetting and mixed wetting (Engelder et al., 2014; Siddiqui et al., 2018).

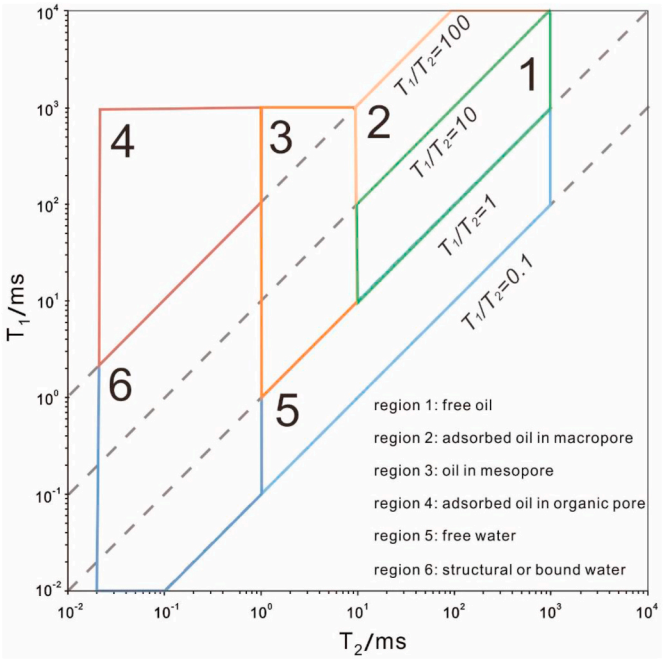

Fig. 9. Locations of each hydrogen-bearing components of shale on T_1-T_2 map with regions: 1-free oil; 2-adsorbed oil in macropore; 3-oil in mesopore; 4-adsorbed oil in organic pore; 5-free water; 6-structural & bound water. The different T_1/T_2 values are indicated by dotted lines.

4. Results

4.1. Basic geological characteristics

4.1.1. Lithological characteristics

X-ray diffraction analysis is used to conduct mineral identification and quantification. The mineral composition of the Fengcheng Fm shale varies widely and mainly consists of calcite (2.2%–62.9%, 15% on average), dolomite (3.4%–92.4%, 24% on average), quartz (3.7%–51.8%, 22% on average), feldspar (2.4%–46.2%, 21% on average), and small amounts of clay minerals (0–31.1%, 8% on average), pyrite (0–17.5%, 5% on average) and other minerals (average 5%), such as zeolites and gypsum. From the edge to the center of deposition, the average carbonate mineral content increases from 46% to 54%, the average siliceous mineral content decreases from 45% to 24%, and the average clay content decreases from 8.7% to 6.4%.

Mineral characteristics can be clearly described under SEM. Dolomite and calcite are granular in the matrix, but calcite is more stratified in microfractures (Fig. 3a and b). Autogenic granular quartz particles are embedded among minerals (Fig. 3c), tabular albite grows in an aggregate manner (Fig. 3d), and clay minerals are mainly montmorillonite and illite/montmorillonite mixed layers (Fig. 3e). Pyrite is often distributed as aggregates and granules (Fig. 3f). A small amount of short columnar gypsum (Fig. 3g) and columnar zeolites (Fig. 3h) are present. A large number of alkaline minerals, such as reedmergnerite (Fig. 3i), wegscheiderite and shortite, were found in Mbr 1 of the Fengcheng Fm near the deposition center.

The lithofacies of the Fengcheng Fm shale can be classified as siliceous shale, calcareous shale and mixed shale, while clay shale is not developed (Fig. 4). The clay content of the mixed shale is generally greater than 10%, the clay content of the siliceous shale is lower, and the calcareous shale basically contains no clay.

4.1.2. Organic geochemistry

The basic geological information is shown in Fig. 5 and Table 1. The TOC content varies in the range of 0.14–2.95 wt% with an average of 1.06% (Table 1). The hydrogen index (HI = S_2/TOC × 100) varies in the range of 126–674 mg HC/g TOC with an average of 324 mg HC/g TOC (Fig. 5a). The HI vs. Tmax and S_2 vs. TOC plots indicate that the shale features Type I/II kerogen but is dominated by Type II, involving kerogen transformation of bacteria and algae (Wang et al., 2015; Zhi et al., 2021). A few samples are biased toward Type III kerogen, which is mainly derived from gas-producing plant fragments (Fig. 5b).

Tmax reflects a low maturity (Ro = 0.5%) due to the heavy oil in pyrolysis parameter S_2, which is inconsistent with the mature thermal evolution stage with a Ro of approximately 1.2% reported in the literature (Cao et al., 2020; Xia et al., 2020; Wang et al., 2021). The whole Fengcheng Fm has high hydrocarbon generation potential and is a high-quality source rock (Fig. 5c). Exploration of the Fengcheng Fm also shows considerable shale oil resource potential (Hu et al., 2016; Zhi et al., 2016, 2021; Wang et al., 2018 ; Tang et al., 2021).

4.2. Characteristics of reservoir and fluid of different lithofacies

4.2.1. Reservoir characteristics

Fig. 6 shows the T_2 spectra of shale with 100% oil saturation (purple solid line), centrifuged (red solid line) and dried (yellow solid line). The number of peaks in the T_2 spectra of oil-saturated rocks reflects pore types. By comparing the pore diameter distribution of high-pressure

Table 3
Contents of free oil, restricted oil, adsorbed oil and total oil expressed by NMR, routine pyrolysis and MIS pyrolysis.

Sample ID	Lithofacies	Free oil		Restricted oil		Adsorbed oil		Total oil		
		mg/g Rock								
		$S_{1\text{-}1}$	Region 1	$S_{1\text{-}2}$	Region 2 + 3	$S_{2\text{-}1}$	Region 4	S_1	$S_{1\text{-}1}$+$S_{1\text{-}2}$+$S_{2\text{-}1}$	Region 1–4
J-5	Siliceous shale	0.03	0.13	1.00	2.73	0.95	2.05	1.09	1.98	4.92
BJ-14		0.25	0.44	2.78	3.96	1.29	1.23	3.21	4.32	5.64
BJ-20		0.07	0.21	0.45	1.75	0.49	1.27	0.97	1.01	3.23
BJ-21		0.11	1.32	0.57	3.56	0.81	0.87	0.57	1.49	5.75
BJ-8		1.52	2.94	6.91	3.90	1.89	1.03	6.91	10.32	7.87
BJ-4		1.59	7.52	11.72	7.64	3.73	1.20	8.39	17.04	16.36
J-9	Calcareous shale	0.18	0.14	1.27	1.69	0.68	0.78	0.53	2.13	2.60
J-28		0.02	0.07	0.43	1.97	0.21	1.70	0.67	0.66	3.74
J-7		0.13	0.18	0.66	2.35	1.07	2.32	0.83	1.86	4.84
BJ-12		0.18	0.16	0.48	1.75	0.68	2.42	0.60	1.34	4.34
BJ-13		0.23	0.21	0.80	1.42	0.83	1.37	1.15	1.86	3.00
BJ-1		0.55	0.32	2.98	3.20	2.87	4.08	4.03	6.40	7.60
J-13		0.51	0.40	0.73	1.66	5.03	3.02	0.91	6.27	5.09
J-15	Mixed shale	0.00	0.00	0.00	0.68	0.01	0.53	0.35	0.01	1.21
J-22		0.00	0.00	0.03	0.62	0.01	1.57	0.43	0.04	2.18
J-12		0.56	0.20	2.87	2.80	1.64	1.93	2.48	5.07	4.93
BJ-18		0.40	0.17	3.27	0.41	2.36	2.48	0.57	3.06	6.03

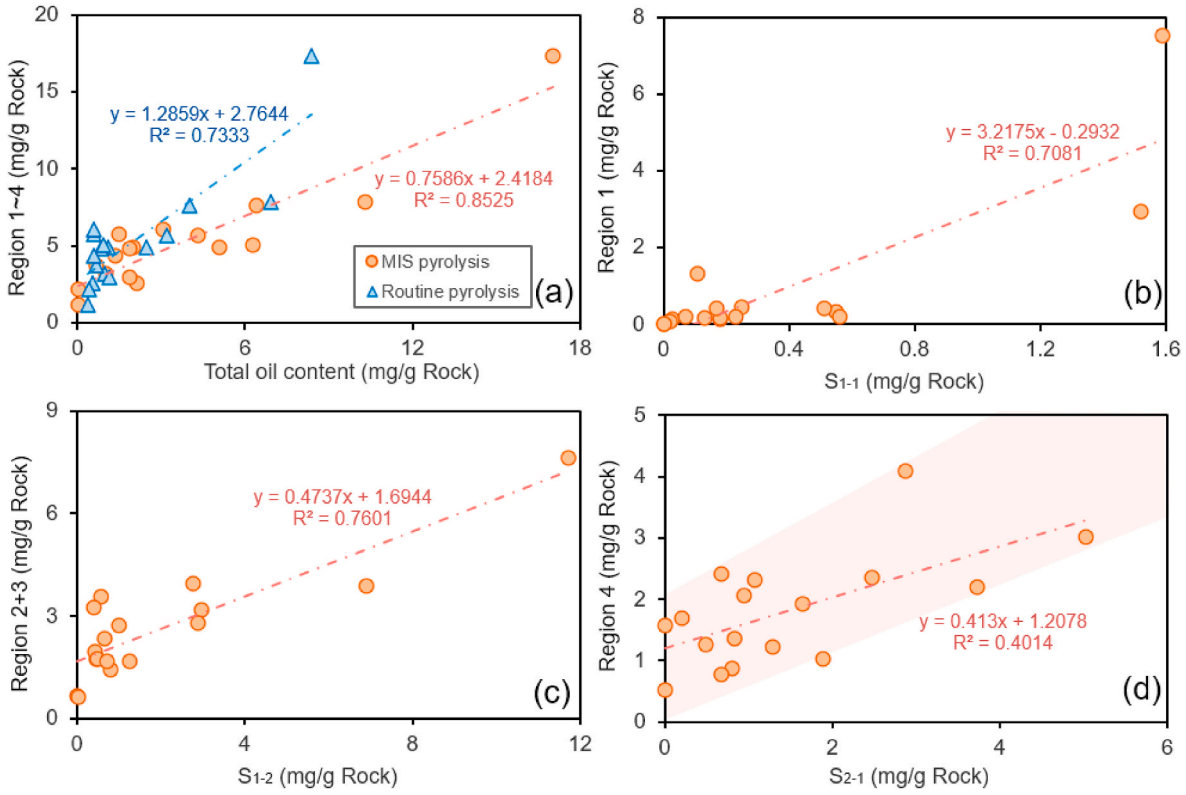

Fig. 10. Comparison of the oil content results by NMR T_1-T_2 map and pyrolysis of the native state samples. The oil content results are subdivided into total oil content (S_1, $S_{1\text{-}1}$+$S_{1\text{-}2}$+$S_{2\text{-}1}$, regions 1–4), free oil content ($S_{1\text{-}1}$, region 1), restricted oil content ($S_{1\text{-}2}$, region 2 + 3) and adsorbed oil content ($S_{2\text{-}1}$, region 4).

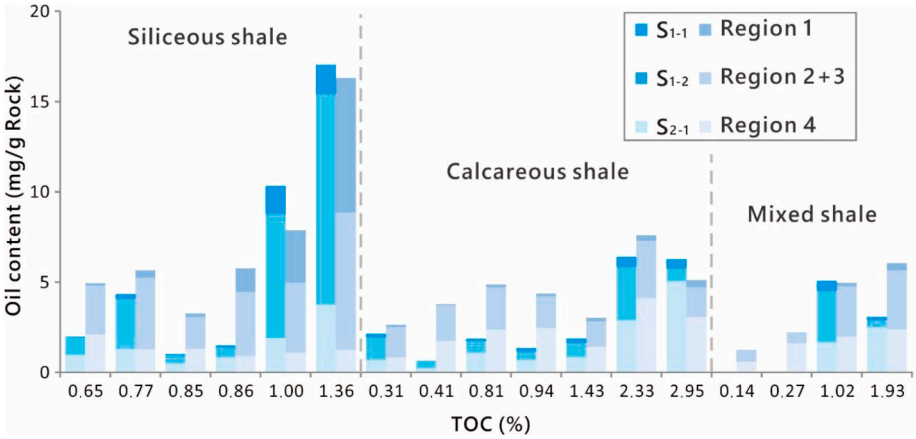

Fig. 11. Comparison of movable oil content of NMR and MIS pyrolysis. Samples are divided by lithofacies, and each type was arranged by TOC from lowest to highest.

mercury injection and T_2 spectrum, the relationship between pore diameter (d) and T_2 in the Fengcheng Formation shale can be expressed as:

$$d = 10 \times T_2^{0.8} \quad (3)$$

The T_2 spectrum can be converted to the pore diameter distribution by Eq. (3) (e.g., Fig. 14a, e, i). The pore diameter distributions of the three types of lithofacies are shown in Table .2, and the pore diameter classification is based on reference to Rouquerol et al. (1994). The T_2 peak area is directly correlated with the pore volume of the sample (Kleinberg et al., 1993; Dunn et al., 2002; Liu et al., 2020). SEM images were used to show the morphology and number of pores at different types (Fig. 7).

The T_2 spectra of oil-saturated shale samples generally have three peaks, named P_1 (<1 ms), P_2 (1–20 ms), and P_3 (>20 ms), in order of increasing T_2 (Li et al., 2015; Zhang et al., 2019). The T_2 spectra of the three lithofacies can be divided into unimodal, bimodal and trimodal distributions.

The T_2 spectrum of siliceous shale is a unimodal distribution with a prominent and high amplitude P_3 (Fig. 6a and b), exhibiting a single pore type. Siliceous shale has a large pore space, with 66.43% of the volume ratio of macropore and only 1.88% of micropore (Table 2). Intergranular pores and intercrystalline pores associated with clastic particles and crystals (carbonate and pyrite) are the main pore types. Abundant irregular polygonal intergranular pores were observed microscopically (e.g., Fig. 7a and e, Fig. 14b and d). Such rigid particles

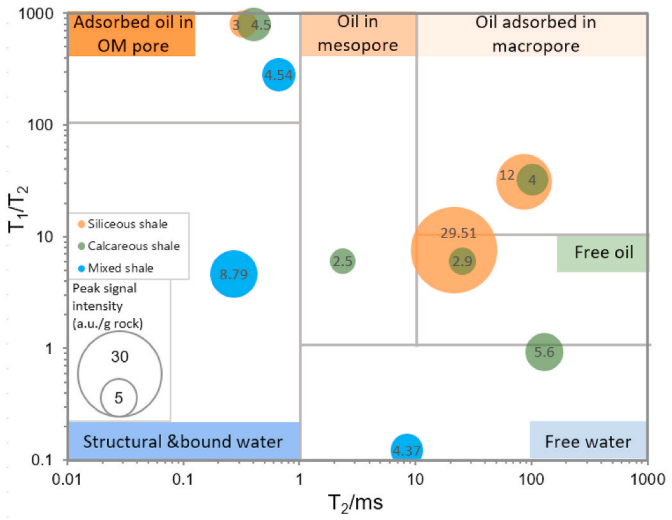

Fig. 12. Distribution of peak signal intensity values in T_1-T_1/T_2 figure of three types of lithofacies. The signal intensity is shown by the area of the circle. The six regions are divided based on the distribution scheme of the T_1-T_2 map.

effectively resist compaction and support sufficiently large pores. In addition, dissolution pores also contribute to the pore space, but on a small scale (Fig. 7c and d).

The T_2 spectra of calcareous shale are bimodally or trimodally distributed (Fig. 6c and d) due to the complex pore system. The amplitude is lower than siliceous shale. P_3 is significantly lower and P_2 is prominent. Sometimes P_1 and P_2 are combined into P_1+P_2 (Fig. 6d). Mesopore has a volume ratio of 58%, and the second is macropore (Table 2). It is dominated by dissolution pores within subrounded, serrated grains, generally <300 nm, with few larger pores under electron microscopy (e.g., Fig. 14f and h). Although the primary deposited calcite formed intercrystalline pores of a certain scale, most of them formed in association with dolomite during diagenesis, hence the multiple rings on the edge (e.g., Fig. 14f and h). Moreover, calcite is prone to reprecipitate and fill primary intergranular and intercrystalline pores, blocking part of the pore throats due to CO_3^{2-}-rich formation water (Li et al., 2019, 2020a, b; Li et al., 2020b) (Fig. 7b). These processes further reduce the pore volume. Densely distributed elliptical pores inside soluble minerals are formed by dissolution; they are completely preserved and become the main contributors to pore space, together with residual intergranular and intercrystalline pores.

Mixed shale has significantly higher P_1 than the other peaks (Fig. 6e and f), reflecting a single pore type and poor connectivity. Among the three lithofacies, the highest volume ratio of mesopore and micropore is found in mixed shale, with 66.68% and 18.51%, respectively (Table 2). Abundant clay minerals were observed, developing lamellar intracrystalline pores (e.g., Fig. 7f, Fig. 14j and l). The pore widths are generally less than 400 nm and up to 1.2 μm. However, these clay minerals fill intergranular and intracrystalline pores, causing the pore system to become narrow and occluded (e.g., Fig. 14j and l). Therefore, the samples mainly develop exhibit clay intracrystalline pores, with a few intergranular pores and dissolution pores.

For siliceous shale, calcareous shale and mixed shale, the dominant peaks show a gradual transition from P_3 to P_1 (Fig. 6), with pore diameters changing from predominantly macropore to predominantly mesopore and micropore (Table 2). The pore system changes from large intergranular pores and intercrystalline pores to intracrystalline pores and clay intragranular pores. The connectivity of intragranular dissolution pores is poor, while intergranular pores are more easily interconnected. Organic pores are often rich in hydrocarbons. Microfractures with the participation of organic matter are preferred channels for crude oil percolation, with widths up to 2 μm, which can further connect

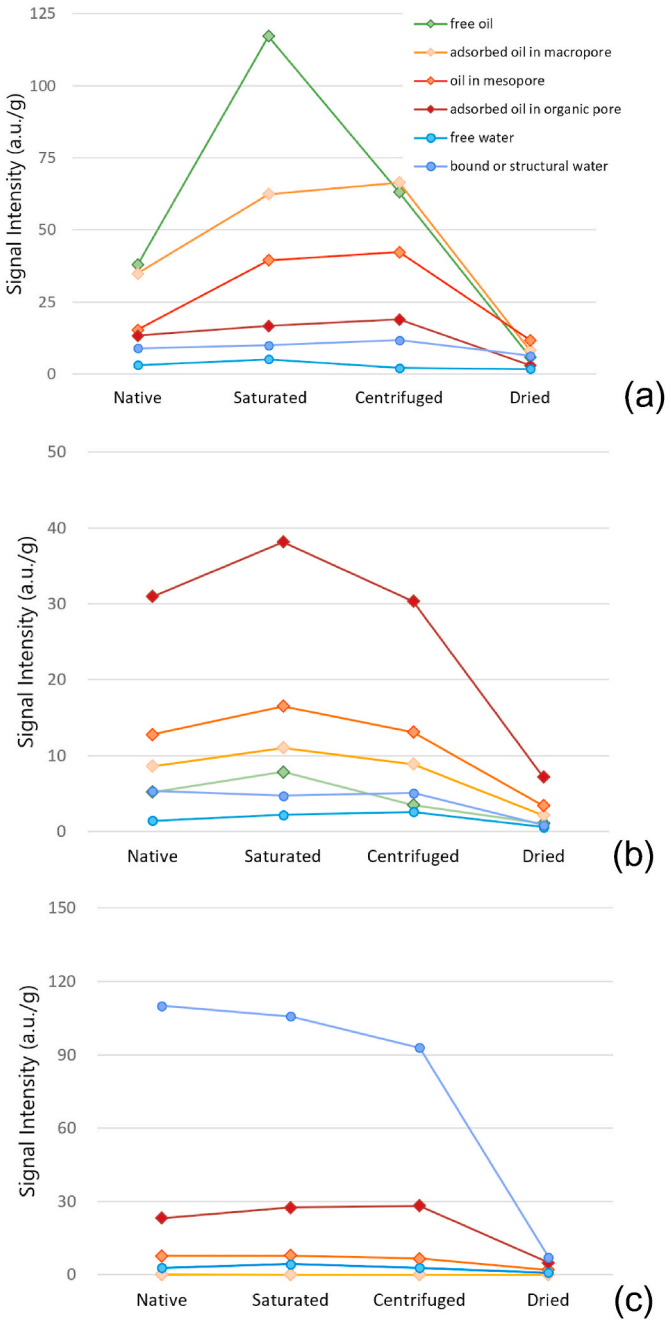

Fig. 13. Cumulative signal intensity of the scheme regions for the target rock samples (a-siliceous shale; b-calcareous shale; c-mixed shale) at four saturation states.

various types of pores in shale reservoirs and increase the connectivity of the pore system (e.g., Fig. 7g and h, Fig. 15). Intergranular pores and intercrystalline pores, microfractures and organic matter pores are important pore spaces for oil and gas accumulation in the shales of the Fengcheng Fm.

4.2.2. Fluid characteristics

The T_1-T_2 maps of different shale types are significantly different, showing great differences in type, content, and state of fluid. Fig. 8 shows the T_1-T_2 maps of three samples in native, saturated, centrifuged, and dry states. The color table provides the association between color and signal intensity and has been adjusted to be consistent in the same samples. Noisy signals during data inversion exist at the edges of the T_1-T_2 map and have no practical significance.

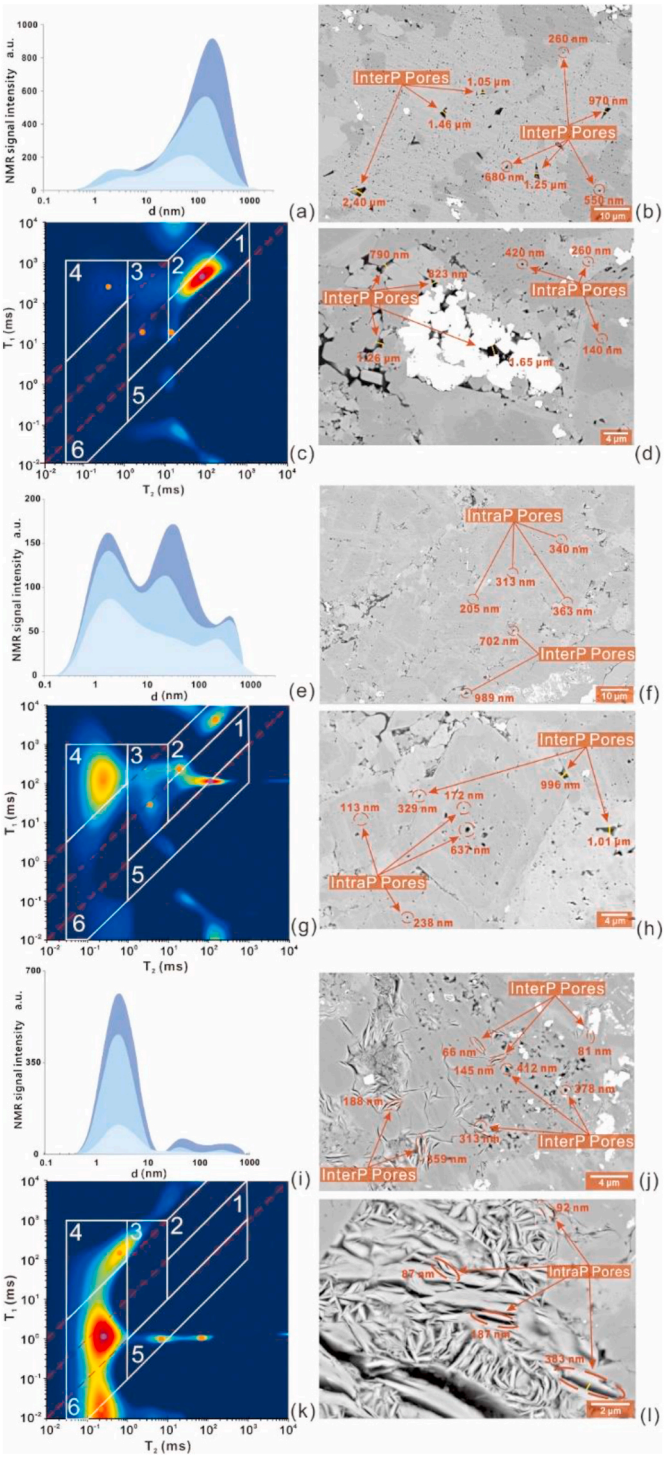

Fig. 14. NMR T_2 spectra (a, e, i) at oil saturation state, centrifuged stateand dried state,T_1-T_2 map (c, g, k) at oil saturation state, and SEM (b, d, f, h, j, l) showing the mineral composition, pore structureand movability for three types of lithofacies. (a–d) Siliceous shale, sample ID: BJ-8. (e–h) Calcareous shale, sample ID: J-13. (i-l) Mixed shale, sample ID: J-22. InterP = interparticle; IntraP = intraparticle.

In the native state, a signal point with the highest intensity was observed at $T_2 = 20$ ms and $T_1/T_2 = 8$ in siliceous shale (Fig. 8A1-A4) as the dominant signal (purple point). The other two insignificant signal points (orange point) are characterized by $T_2 = 80$ ms, $T_1/T_2 = 33$ and $T_2 = 0.3$ ms, $T_1/T_2 = 700$. These are residual oil signals in the sample (Nicot et al., 2016). After the sample was saturated with oil, the dominant signal point moved to the upper right of the map ($T_2 = 100$ ms) and the amplitude was significantly enhanced. After centrifugation, the dominant signal was significantly reduced, and the remaining signal was concentrated at $T_2 = 50$ ms. This indicates that the main region where the movable oil signal is displayed is $T_2 > 10$ ms. The other two signals have different behaviors after centrifugation. They remained in place (signal point at $T_2 = 110$ ms, $T_1/T_2 = 33$) and moved to the lower left (signal point at $T_2 = 5$ ms, $T_1/T_2 = 3$). It is likely that the centrifugal process redistributed the oil in the pore space. Part of the oil is adsorbed on the surface of macropores and is difficult to throw out, and the other part of the oil is pressed into narrow pores by centrifugal force.

Native-state calcareous shale samples (Fig. 8 B1–B4) have more signals with a wider distribution, showing complex fluid composition. The T_1/T_2 of these signals are 1, 9, 33, and 600, respectively. Two signals of different T_2 are distributed on the line of $T_1/T_2 = 9$. The dominant signal is located at $T_2 = 100$ ms and $T_1/T_2 = 1$, which seems to be water, but T_2 is too high (Fleury and Romero-Sarmiento, 2016; Li et al., 2018). Its overlap with an oil signal point on the $T_1/T_2 = 9$ line. After saturation, the dominant signal and the point at $T_1/T_2 = 600$ are enhanced. The signal increases in the region of $T_2 = 1$–100 ms. After centrifugation, the signal intensity of all points decreases and is slightly lower than that of the native state. The points of dominant signal and $T_1/T_2 = 600$ decrease significantly.

These features suggest that the signals in the T_1-T_2 map of calcareous shale are closely related to oil. The dominant signal is likely to be generated by oil and water together, such as the fluids in mixing wetted pores. In the region of $T_2 > 1$ ms, the shorter T_2 is, the more signal is retained after centrifugation, indicating that oil movability in this region is mainly influenced by pore size. It is a signal of oil in inorganic pores. Note that the two signal points at $T_2 = 20$ ms and $T_2 = 110$ ms on line $T_1/T_2 = 33$ are joined together after centrifugation, further demonstrating the redistribution effect. Kerogen and bitumen have extremely fast decay rates with a shorter T_2 (<1 ms) due to a strong homonuclear dipole-coupling interaction (Kausik et al., 2017; Li et al., 2018; Khatibi et al., 2019). However, the signal intensity in this region increases and then decreases after saturation and centrifugation. It is presumed that there is oil adsorbed on the surface of the solid organic matter and organic pores in this region.

The T_1-T_2 map of the mixed shale sample in the native state (Fig. 8 C1–C4) is very different from that of the other samples. Signals are distributed on the left and lower part of the T_1-T_2 map. The dominant signal is located at $T_2 = 0.3$ ms and $T_1/T_2 = 4$. The other two signals are located at $T_1/T_2 = 200$ and $T_1/T_2 < 1$. Two minor signals are located at $T_2 = 10$ ms and $T_2 = 90$ ms, respectively. After saturation and centrifugation, the signals in the region of $T_1/T_2 < 100$, $T_2 < 1$ ms and $T_2 =$ 4–100 ms are almost constant but disappear after drying, indicating a water signal. The former is bound water adsorbed on the surface of hydrophilic clay particles with a large specific surface area (Korb et al., 2014; Li et al., 2018), and the latter is water remaining in the pore. However, the amplitude of the signal points at $T_1/T_2 = 200$ and $T_2 =$ 0.1–2 ms was enhanced and then weakened, indicating that they are adsorbed oil and a small amount of solid organic matter.

The signals in all T_1-T_2 maps in the dry state were substantially reduced, but a small amount of signal remained (Fig. 8 A4, B4, C4). For siliceous shale, the remaining signal is in the center of the T_1-T_2 map, probably because the extraction process was unable to remove the residual oil from the original dead pores in the sample (Li et al., 2018). Compared to siliceous shale, the dry sample of calcareous shale has more signals in the short T_2 region (0.1–1 ms). This is related to the large content of kerogen and bitumen in this sample, as they are insoluble in the extraction solvents (Gutman et al., 2017). The remaining signal of the mixed shale is in the lower left part of the map and belongs to structural water molecules existing in the space between the adjacent crystal layers of clay minerals.

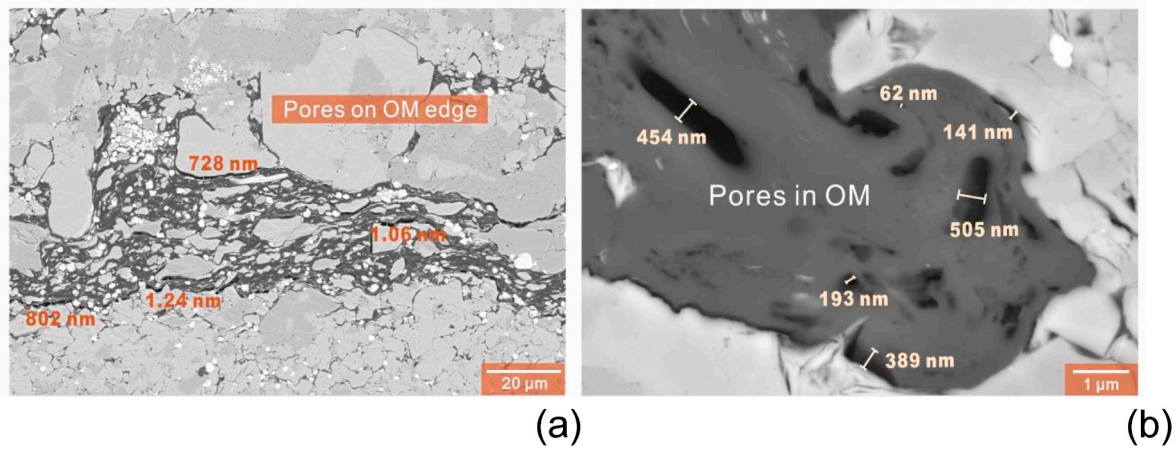

Fig. 15. Organic matter (OM) pores in the Fengcheng Fm shale. (a) Layered organic matter, sample ID: J-13. (b) Dispersed organic matter, sample ID: J-22.

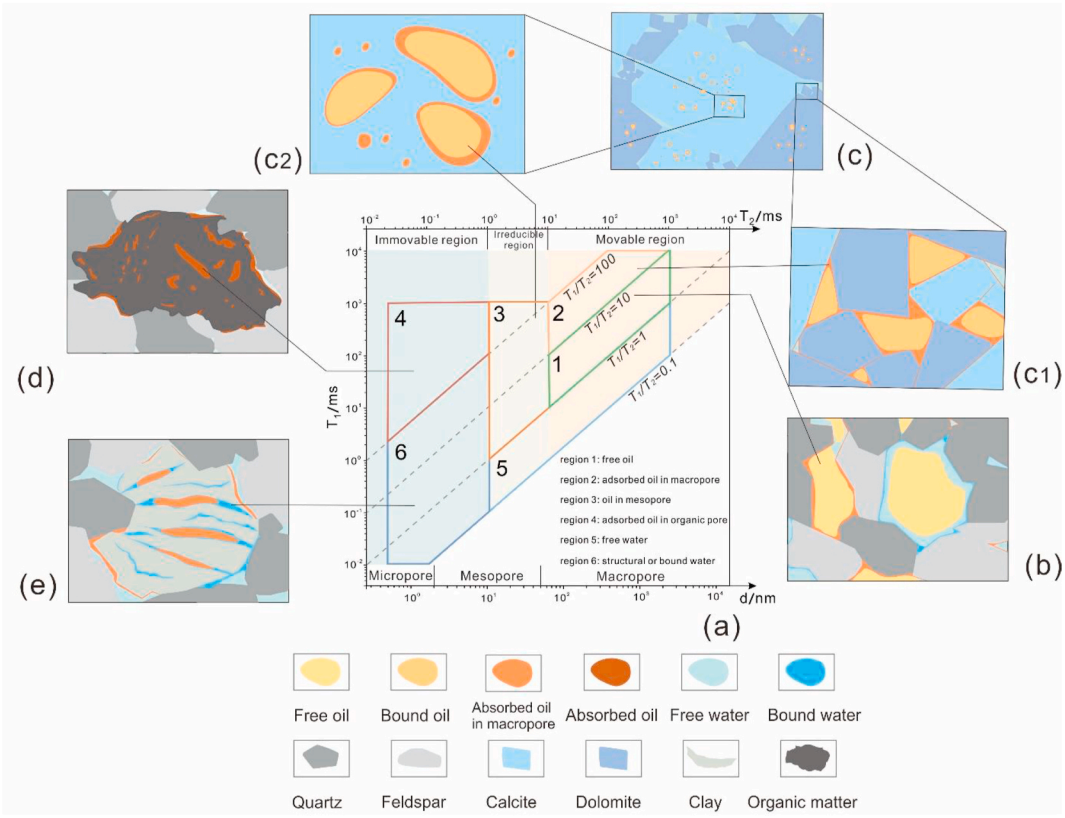

Fig. 16. Occurrence model of shale oil by NMR. (a) NMR T_1-T_2 map representing the pore system, movability and composition of fluid; (b) free oil and adsorbed oil occurs in intergranular pores of clastic particles; (c) oil occurs (c2) between carbonate crystals and (c1) in carbonate crystals with small amount of adsorbed oil; adsorbed oil is abundant in (d) organic matter and bound water in intragranular pores of (e) clay mineral.

5. Discussion

5.1. Fluid identification of NMR

5.1.1. T_1-T_2 map interpretation scheme

For better fluid classification, a T_1-T_2 map interpretation scheme (Fig. 9) was proposed for the shale samples. This scheme is based on the studies of Li et al. (2018) and Mukhametdinova et al. (2021), as well as on the T_1-T_2 map observations of samples with different saturations in this study.

According to the description of the NMR response variation above, rich information on the distribution of the fluid signal in the T_1-T_2 map was obtained. a) The oil signal in inorganic pores is distributed in the region of $T_2 > 1$ ms. b) Oil–water mixed fluids appear near line $T_1/T_2 = 1$. c) The free oil signal is mainly present in region 1. Region 2 probably indicates oil adsorbed on the oil wettability surfaces of minerals. The short T_2 (1–10 ms) of the signal in region 3 indicates the presence of oil in the mesopores. d) The signal in region 4 shows high molecular weight and strong surface relaxation ($T_1/T_2 > 100$), indicating a strong attraction of the oil to solid organic matter. Note that the kerogen and bitumen signals (Kausik et al., 2017) may also be located in this region. e) For water, free water signals are usually distributed in region 5 (Fleury and Romero-Sarmiento, 2016; Khatibi et al., 2019; Mukhametdinova et al., 2021). Region 6 contains both adsorbed water on the

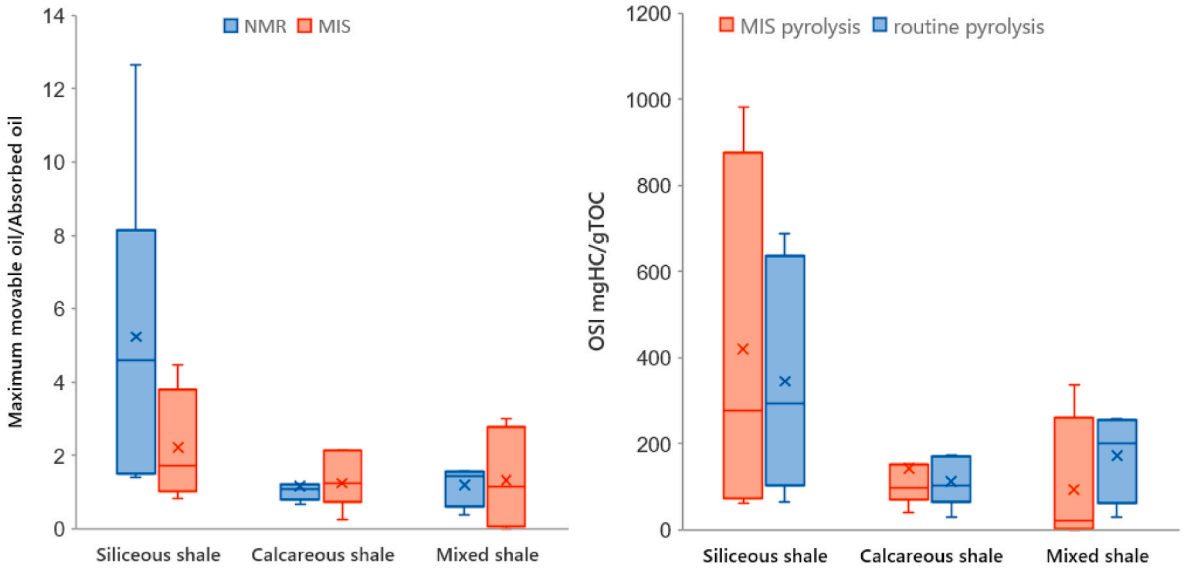

Fig. 17. Comparison of movability parameters of NMR, MIS, and routine pyrolysis. Parameters include ratio of maximum movable oil and adsorbed oil and OSI (oil saturation index = S_1/TOC × 100).

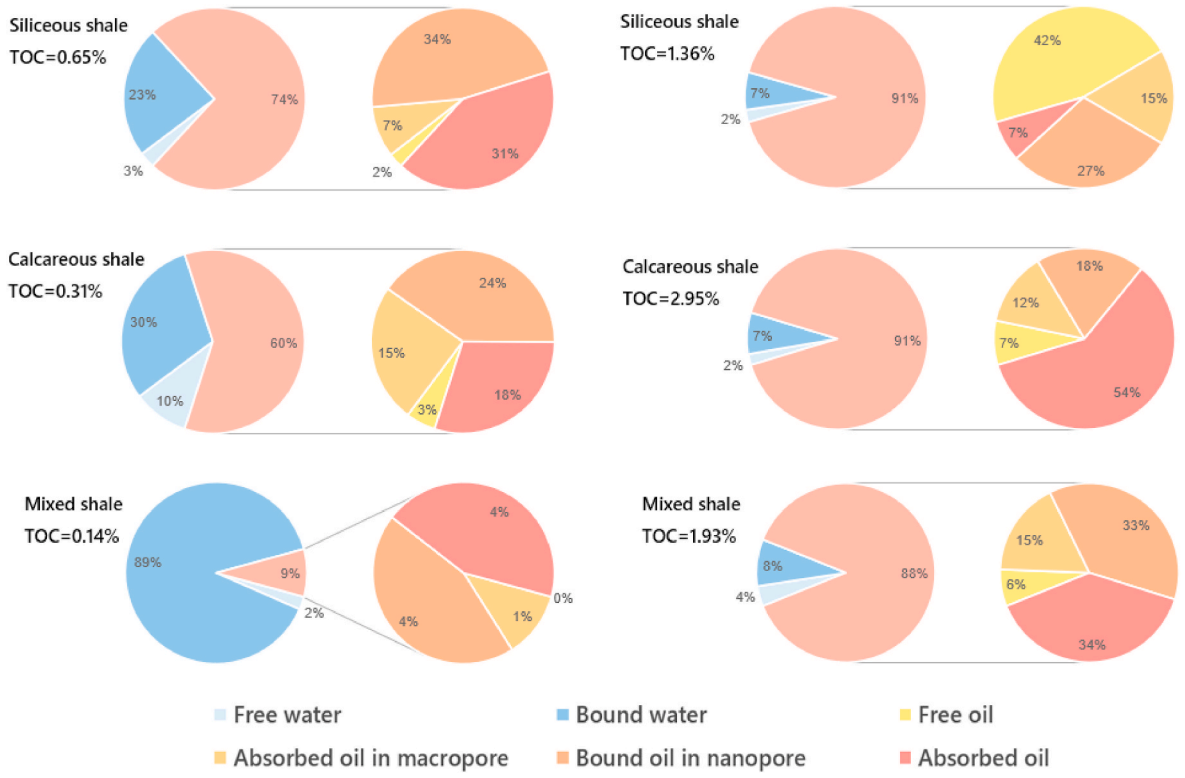

Fig. 18. Comparison of fluid saturation and movable oil saturation in NMR of three lithofacies. The saturation of high and low TOC samples was compared in each lithofacies.

surface of clay and structural water in the crystal lattice of clay minerals ($T_1/T_2 < 1$).

Thus, the new T_1-T_2 fluid type partition consists of the following six regions. Region 1: free oil, T_1/T_2 = 1–10, and T_2 = 10–1000 ms; region 2: oil adsorbed in macropores, T_2 is the same as region 1, but T_1/T_2 = 10–100; region 3: oil in mesopores, $T_1/T_2 > 1$, T_2 = 1–10 ms; region 4: oil adsorbed in organic pores, $T_1/T_2 > 100$ and $T_2 < 1$ ms; region 5: free water, T_1/T_2 = 0.1–1 and T_2 = 1–1000 ms; region 6: structural or bound water, T_1/T_2 = 0.1–100, $T_2 < 1$ ms.

Li et al. (2018) suggested that adsorbed oil mainly exists at 0.1 ms < T_2 < 1 ms and kerogen exists near T_2 = 0.1 ms in T_1-T_2 map, which is consistent with the region 4 proposed in this study. In our experiments, the signals of the two overlapped and were difficult to separate. Therefore, we combined them into one region. However, the distribution of oil signals in the T_1-T_2 map of the Fengcheng Fm shale is complex. Due to the development of microfractures and macropores, the oil in them has a longer relaxation time, which makes the T_2 of the oil signal close to 1000 ms at most. In addition, this study further classifies the oil

components with $T_2 > 1$ ms: 1) The division of region 2 is due to the oil wettability of some macropores and microfractures which makes a part of light oil adsorbed on their surface because the higher T_1/T_2 ($10 < T_1/T_2 < 100$) indicates a stronger surface relaxation effect (Siddiqui et al., 2018). 2) Region 3 is delineated because this part of oil exists in smaller pore spaces such as mesopores, and the capillary forces make it difficult for the oil to be released.

5.1.2. Connection between NMR and pyrolysis parameters

Table 3 shows the contents of free oil, restricted oil, adsorbed oil and total oil expressed by NMR and pyrolysis, respectively. The oil molecules represented by region 2 and region 3 are likely to have similar thermal volatilization properties, although they are subject to different sources of resistance, and are therefore collectively referred to as "restricted oil". The NMR oil content data were derived from the NMR signal intensity data of the native samples by the relationship between known masses of kerosene and signal intensity. For the total oil content results, both routine pyrolysis and MIS pyrolysis showed a high positive correlation with NMR, with the latter having a better correlation with NMR ($R^2 = 0.85$) (Fig. 10a). Routine pyrolysis underestimates oil content since heavy hydrocarbons are detected in the range of the thermal cracking temperature of kerogen (i.e., peak S_2) (Jiang et al., 2016a, b; Zhang et al., 2020).

However, the content of oil in different occurrence states as evaluated by NMR and MIS is differed (Fig. 10b, c and d). Their differences are reflected in three parts: 1) The amount of free oil is higher in NMR than in MIS (Fig. 10b), especially in the siliceous shale (Fig. 11). Pyrolysis experiments require crushing and grinding the sample into powder, which destroys most of the macropores and makes the light hydrocarbons easier to volatilize. In contrast, NMR experiments only require plunger samples, and some light hydrocarbons are retained in the samples (Espitalie et al., 1977; Michael, 2013). 2) Sometimes the restricted oil content of NMR is much higher than that of pyrolysis (Fig. 11). The grinding process of the pyrolysis experiment likewise destroys part of the mesopores, resulting in the escape of the light oil originally blocked by capillary forces. Therefore, $S_{1\text{-}2}$ mainly characterizes the oil adsorbed on the surface of oil-wetted pores, similar to region 2 of NMR. 3) The correlation between the adsorbed oil content of the two methods is not high. This is due to the parameter $S_{2\text{-}1}$ contains resins and asphaltenes in addition to heavy hydrocarbons, both of which are strongly polar and viscous. The homonuclear dipole coupling reaction during the magnetization process caused part of the NMR signal to be missed in region 4 during acquisition using spin–echo sequences. Therefore, the adsorbed oil of NMR will be lower than that of pyrolysis in some samples. In addition, Fengcheng Fm shale includes a large number of alkaline minerals, such as trona and borosilicate (Li et al., 2019; Yu et al., 2019), which contain hydroxyl groups or structural water, and their signals may also appear in region 4 (Fleury and Romero-Sarmiento, 2016).

5.2. Fluid occurrence state, space and mode

The interpretation scheme was applied to the T_1-T_2 map of target rock samples. First, the distribution of peak signal intensity in each region of the T_1-T_2 map in the three shale types in the native state was plotted (Fig. 12). Siliceous shale shows strong signals of free oil and adsorbed oil in macropores. The fluid species in the calcareous shale is complex, containing adsorbed oil in organic pore, free oil, adsorbed oil in macropores, oil in mesopores and some oil mixed with water. In contrast, the bound water and free water signals in the mixed shale are obvious and contain only a small amount of adsorbed oil in organic pore.

The combination of SEM and T_2 spectra reveals oil and water contents, occurrence state and spatial distribution in different lithofacies. The free oil signal of siliceous shale samples increases rapidly to a maximum after saturation with oil and decreases significantly after centrifugation and extraction (Fig. 13a). Low-viscosity oil is present in the intergranular pores of the siliceous shale, mostly macropores (Fig. 14b), and it can easily flow out during high-speed centrifugation. However, not all of the oil is free, and some of the oil adsorbs to the macropore surface (Fig. 14a and c). In addition, some oil is present in the intragranular pores with diameters of approximately 200 nm (Fig. 14d). The trend of the content change of oil in mesopores is similar to that of adsorbed oil in macropores during centrifugation and extraction. This shows that their movability is similar but weaker than that of free oil. In addition, the content of adsorbed oil in macropores and oil in mesopores remained stable after centrifugation, consistent with the observation in the T_1-T_2 map. Only a small amount of fluid is movable because centrifugal force has difficulty overcoming capillary force in mesopores and adsorption of oil wetting pore surfaces, and they can be extracted using polar solvents (Zhu et al., 2021).

The calcareous shale has mainly adsorbed oil. The adsorbed oil signal is enhanced after saturation and decreases to the same extent after centrifugation (Fig. 13b and 14e). Organic-rich layers and dispersed organic matter were found in the calcareous shale. Microfractures of 500 nm–1 μm are developed within organic matter and between inorganic minerals (Fig. 15a). For dispersed organic matter, pores of various sizes are also developed due to the volume expansion of hydrocarbons generated in kerogen during thermal maturation, resulting in the internally dense development of pores ranging from tens to hundreds of nanometers in diameter (Fig. 15b). A portion of oil is pressed into the space in the center of organic pores during saturation. However, the low viscosity and relatively long distance from the organic matter surface make it weakly adsorbed, and it can be removed after centrifugation. In contrast, most of the remaining adsorbed oil is washed out during extraction, and the signal is substantially reduced. Unlike in the siliceous shale, the signal intensity of oil in mesopore in the calcareous shale is strong because of the large number of intracrystalline and intercrystalline pores developed (Fig. 14f and h). Fewer adsorbed oil in macropores and free oil correspond to small number of intergranular pores in this sample.

The contents of free water and bound water remain stable at low values in the two samples above. In contrast, mixed shale samples show a different behavior: bound water contributes the most to the fluid signal at different saturations and decreases substantially in the dried state. The signal of adsorbed oil in organic pore dominates and remains stable during saturation and centrifugation (Fig. 13c). The clay particles develop a large number of lamellar pores inside and have a high specific surface area, so a large amount of bound water adheres to their surface. At the same time, clay blocks the pore throats (Fig. 14j and k), which makes it difficult for oil to be pressed in during saturation. Although some clay grains have larger pore sizes, this is likely a misinterpretation due to clay shrinkage caused by water evaporation from the sample. Under the conditions of high pressure and filled with formation water, the pore size should be much smaller. In summary, clay minerals severely affect the accommodation ability and permeability of reservoirs. Centrifugation removes mainly free water and a small portion of clay-bound water. Subsequently, the extraction-drying evaporated most of the bound water, while structural water escaped at a higher temperature and was retained within the clay.

We constructed a conceptual model (Fig. 16) to illustrate the identification of the occurrence state and spatial distribution of fluid by the T_1-T_2 map. This model considers the movability, including movable fluids (orange region), irreducible fluids (yellow region), and immovable fluids (blue region). The position of micropore, mesopore and macropore in the T_1-T_2 map was also considered (Fig. 16a). Movable fluids are mainly associated with macropores, such as intergranular pores, and are dominated by free oil. Irreducible fluids include oil in mesopores and adsorbed oil in macropores, and the pore types are mainly intracrystalline and intercrystalline pores. The proportion of produced fluids can be increased by changing the conditions during the development process. Adsorbed oil in organic pores is located in the immovable fluid region. There are strong van der Waals and Coulomb

forces between heavy oil molecules and solid organic matter. As a result, the oil barely flows. Therefore, adsorbed oil in organic pores remains in the pores deep in the formation and cannot be extracted by current technology (Nelson, 2009).

5.3. Movability of different lithofacies

Movability can be evaluated by a combination of parameters such as total oil content, ratio of free oil to adsorbed oil, and movable oil saturation. High frequency 2D NMR and MIS pyrolysis, combined with traditional geochemical parameters such as TOC, S_1 and OSI, can accurately characterize the movability of different lithofacies. First, the total oil content can be expressed as the sum of the NMR signal intensity of soluble organic matter per unit rock mass (regions 1–4) and MIS pyrolysis ($S_{1\text{-}1}+S_{1\text{-}2}+S_{2\text{-}1}$). The movability of restricted oil (regions 2+3) increases with increasingly favorable formation or production conditions. Therefore, the sum of free oil and restricted oil can be used as the maximum movable oil volume. The ratio of (regions 1+2+3)/region 4 of NMR can characterize the ratio of movable oil to adsorbed oil, similar to $(S_{1\text{-}1}+S_{1\text{-}2})/S_{2\text{-}1}$ of MIS. NMR can also obtain oil saturation parameters, including oil saturation, free oil saturation and adsorbed oil saturation.

Both NMR and pyrolysis results show that the siliceous shale has superior movability (Fig. 11). Compared to the calcareous shale and mixed shale, the siliceous shale exhibits the highest oil content and movable oil only at TOC = 1.36%. The NMR average total oil content of the siliceous shale is 10 times higher than that of the calcareous shale and 14 times higher than that of the mixed shale. In addition, the average NMR movable oil content of the siliceous shale reaches 5 times the adsorbed oil content (Fig. 17a), and the OSI also shows extremely high production capacity (Fig. 17b). The mixed shale and calcareous shale show lower oil contents, and the average values of both the movable oil ratio and adsorbed oil ratio are close to 1:1.

The oil-bearing saturation of the three lithofacies types with the lowest and highest TOC contents were compared (Fig. 18). When evaluating shale movability, a comprehensive consideration of organic matter abundance, mineral composition, and attention to clay content is needed. When the amount of organic matter is low, the siliceous shale and calcareous shale are predominantly oil-bearing, while the mixed shale contains a large amount of bound water, showing low permeability and poor oil content (Fig. 18a, c and e). The increase in TOC significantly enhances the oil saturation of shale, and finally stabilizes near 90%. The mixed shales change from bound-water dominated to oil-saturated dominated (Fig. 18b, d and f). This is because the increased amount of organic matter usually generates more oil, displacing most of the free and bound water from the pores. Free oil saturation is significantly enhanced in the siliceous shale; adsorbed oil saturation is elevated in the calcareous shale, and the free oil saturation and adsorbed oil in macropore saturation are elevated in the mixed shales.

With the increase in TOC, the movable oil of the siliceous shale is significantly higher, while the calcareous shale and mixed shale mainly show an increase in the adsorbed oil content. This indicates that TOC is a favorable factor for the movability of the siliceous shale. In addition, the siliceous shale has significantly high oil content, low hydrocarbon potential (TOC = 1.36%, HI = 398 mg/g TOC) and high movability. Conversely, the calcareous shale (TOC = 2.9%, HI = 674 mg/g TOC) and the mixed shale (TOC = 1.9%, HI = 644 mg/g TOC) have low oil contents and high hydrocarbon potentials. These contradictions suggest that oil in the siliceous shale reservoirs may be mainly transported in from neighboring formations because such reservoirs have larger pore space and lower transport resistance, and lighter oil is preferentially charged (Li et al., 2016); the organic-rich calcareous shale and mixed shale have high hydrocarbon generation capacity but poor oil-holding space, so the excess oil generated is discharged.

6. Conclusions

Large lacustrine shale oil resources have been found in the organic-rich shale of the Permian Fengcheng Fm in the Mahu Sag, Junggar Basin, NW China. Fengcheng Fm shales are highly heterogeneous, with significant differences in organic matter abundance and mineral composition, which are suitable for the study of differences in fluid occurrence state and movability in different lithofacies. The following insights from this work can be summarized:

A novel T_1-T_2 map fluid region division method is proposed based on the HF-NMR test dataset at different saturations of Fengcheng Fm shale, including free oil (region 1), adsorbed oil in macropores (region 2), oil in mesopores (region 3), adsorbed oil in organic pores (region 4), free water (region 5) and bound water (region 6). Region 1, 2+3 and 4 of the T_1-T_2 map correspond well with $S_{1\text{-}1}$, $S_{1\text{-}2}$ and $S_{2\text{-}1}$ of MIS pyrolysis, respectively. NMR is generally better than MIS pyrolysis in characterizing oil content. Free oil has the strongest movability. Adsorbed oil in macropores and oil in mesopores are jointly called restricted oil, and the sum of free oil and restricted oil can be used as the maximum movable oil amount. Adsorbed oil is immovable under current production conditions.

Siliceous shale is rich in free oil and adsorbed oil in macropores, which are located in the center and edge of intergranular/intercrystalline pores, respectively. The calcareous shale features a large amount of adsorbed oil on the surface and internal pores of dispersed organic matter, as well as the marginal fracture of organic matter laminae. The mixed shale features a large number of narrow and isolated clay intergranular pores and contains a large amount of bound water. Siliceous minerals are favorable to free oil occurrence, and calcareous minerals have limited holding capacity and mainly contain adsorbed and bound oil. The mixed shale with low organic abundance and high clay content (>10%) contains almost only bound water.

The increase in organic matter abundance is favorable for improving the oil content and permeability of shale and increasing the saturation of movable oil in the siliceous shale and mixed shale and adsorbed oil in the calcareous shale.

Declaration of competing interest

We declare that we do not have any commercial or associative interest that represents a conflict of interest in connection with the work submitted.

Data availability

Data will be made available on request.

Acknowledgments

This study was financially supported by the National Natural Science Foundation of China (41872128, 42202133) and the Strategic Cooperation Technology Projects of CNPC and CUPB (ZLZX2020-01-05).

References

Altawati, F., Emadi, H., Pathak, S., 2021. Improving oil recovery of Eagle Ford shale samples using cryogenic and cyclic gas injection methods - an experimental study. Fuel 302 (5), 121170.

Anderson, R.L., Ratcliffe, I., Greenwell, H.C., Williams, P.A., Cliffe, S., Coveney, P.V., 2010. Clay swelling — a challenge in the oilfield. Earth Sci. Rev. 98 (3–4), 201–216.

Birdwell, J.E., Washburn, K.E., 2015. Multivariate analysis relating oil shale geochemical properties to NMR relaxometry. Energy Fuel. 29 (4), 2234–2243.

Bloembergen, N., Purcell, E.M., Pound, R.V., 1948. Relaxation effects in nuclear magnetic resonance absorption. Phys. Rev. 73.

Cao, J., Xia, L., Wang, T., Zhi, D., Tang, Y., Li, W., 2020. An alkaline lake in the Late Paleozoic Ice Age (LPIA): a review and new insights into paleoenvironment and petroleum geology. Earth Sci. Rev. 202, 103091.

Carr, H.Y., Purcell, E.M., 1954. Effect of diffusion on free precession in nuclear magnetic resonance experiments. Phys. Rev. 94 (3), 630–638.

Clark, A.J., 2009. SPE Annual Technical Conference and Exhibition. OnePetro.
Coates, G., Xiao, L., Prammer, M., 2007. Principle and Application of NMR Logging. Petroleum industry press.
Curtis, J.B., 2002. Fractured shale-gas systems. AAPG Bull. 86 (11), 1921–1938.
Daigle, H., Johnson, A., Thomas, B., 2014. Determining fractal dimension from nuclear magnetic resonance data in rocks with internal magnetic field gradients. Geophysics 79 (6), D425–D431.
Davis, L.A., 2018. The shale oil and gas revolution. Engineering. 4 (4), 438–439.
Díaz-Pérez, A., Cortés-Monroy, I., Roegiers, J.C., 2007. The role of water/clay interaction in the shale characterization. J. Petrol. Sci. Eng. 58 (1–2), 83–98.
Dunn, K.J., Bergman, J.D., Latorraca, A.G., 2002. Nuclear Magnetic Resonance: Petrophysical and Logging Applications. Nuclear Magnetic Resonance Petrophysical and Logging Applications.
Engelder, T., Cathles, L.M., Bryndzia, L.T., 2014. The fate of residual treatment water in gas shale. J. Unconv. Oil Gas Res. 7, 33–48.
Espitalie, J., Madec, M., Tissot, B., Mennig, J.J., Leplat, P., 1977. Source rock characterization method for petroleum exploration. Preprint Offshore Technol. Conf. (9), 439–444.
Fleury, M., Romero-Sarmiento, M., 2016. Characterization of shales using T1–T2 NMR maps. J. Petrol. Sci. Eng. 137, 55–62.
Ge, X., Myers, M.T., Liu, J., Fan, Y., Zahid, M.A., Zhao, J., Hathon, L., 2021. Determining the transverse surface relaxivity of reservoir rocks: a critical review and perspective. Mar. Petrol. Geol. 126, 104934.
Gentzis, T., Carvajal-Ortiz, H., Harry Xie, Z., Hackley, P.C., Fowler, H., 2021. An integrated geochemical, spectroscopic, and petrographic approach to examining the producibility of hydrocarbons from liquids-rich unconventional formations. Fuel 298, 120357.
Gutman, I.S., Potemkin, G.N., Postnikov, A.V., Postnikova, O.V., Kozlova, E.V., Alekseev, A.D., Karpov, I.A., 2017. Methodical approaches to the reserves and resources estimation of Bazhenov formation (Russian). Neftyanoe khozyaystvo-Oil Ind. 2017 (3), 28–32.
Hu, T., Pang, X., Yu, S., Wang, X., Pang, H., Guo, J., Jiang, F., Shen, W., Wang, Q., Xu, J., 2016. Hydrocarbon generation and expulsion characteristics of Lower Permian P1 f source rocks in the Fengcheng area, northwest margin, Junggar Basin, NW China: implications for tight oil accumulation potential assessment. Geol. J. 51 (6), 880–900.
Hu, T., Pang, X., Jiang, F., Wang, Q., Liu, X., Wang, Z., Jiang, S., Wu, G., Li, C., Xu, T., et al., 2021. Movable oil content evaluation of lacustrine organic-rich shales: methods and a novel quantitative evaluation model. Earth Sci. Rev. 214, 103545.
Hui, J., Sonnenberg, S.A., 2013. Unconventional Resources Technology Conference.
Jarvie, D.M., 2012a. Shale resource systems for oil and gas: Part 1-Shale-gas resource systems. Aapg Memoir 97, 69–87.
Jarvie, D.M., 2012b. Shale resource systems for oil and gas: Part 2-Shale-oil resource systems. Aapg Memoir 97, 89–119.
Jarvie, D.M., Hill, R.J., Ruble, T.E., Pollastro, R.M., 2007. Unconventional shale-gas systems: the Mississippian Barnett Shale of north-central Texas as one model for thermogenic shale-gas assessment. AAPG Bull. 91 (4), 475–499.
Jiang, C., Chen, Z., Mort, A., Milovic, M., Robinson, R., Stewart, R., Lavoie, D., 2016a. Hydrocarbon evaporative loss from shale core samples as revealed by Rock-Eval and thermal desorption-gas chromatography analysis: its geochemical and geological implications. Mar. Petrol. Geol. 70, 294–303.
Jiang, Q., Li, M., Qian, M., Li, Z., Li, Z., Huang, Z., Zhang, C., Ma, Y., 2016b. Quantitative characterization of shale oil in different occurrence states and its application. Petrol. Geol. Exp. 38 (6), 842–849.
Jin, L., Hawthorne, S., Sorensen, J., Pekot, L., Kurz, B., Smith, S., Heebink, L., Herdegen, V., Bosshart, N., Torres, J., 2017. Advancing CO2 enhanced oil recovery and storage in unconventional oil play-Experimental studies on Bakken shales. Appl. Energy 208 (dec.15), 171–183.
Katz, B.J., 1990. Controls on distribution of lacustrine source rocks through time and space. AAPG Memoir 50, 61–76.
Katz, B., Fang, L., 2014. Lacustrine basin unconventional resource plays: key differences. Mar. Petrol. Geol. 56 (3), 255–265.
Kausik, R., Fellah, K., Feng, L., Freed, D., Simpson, G., 2016. High- and Low-Field NMR relaxometry and diffusometry of the bakken petroleum system. In: SPWLA 57th Annual Logging Symposium.
Kausik, R., Fellah, K., Feng, L., Simpson, G., 2017. High-and low-field NMR relaxometry and diffusometry of the bakken petroleum system. Petrophysics-SPWLA J. Form. Eval. Reser. Descr. 58 (4), 341–351.
Khatibi, S., Ostadhassan, M., Xie, Z.H., Gentzis, T., Bubach, B., Gan, Z., Carvajal-Ortiz, H., 2019. NMR relaxometry a new approach to detect geochemical properties of organic matter in tight shales. Fuel 235, 167–177.
Kleinberg, R.L., Straley, C., Kenyon, W.E., Akkurt, R., Farooqui, S.A., 1993. Spe Technical Conference & Exhibition.
Korb, J., Nicot, B., Louis-Joseph, A., Bubici, S., Ferrante, G., 2014. Dynamics and wettability of oil and water in oil shales. J. Phys. Chem. C 118 (40), 23212–23218.
Larter, S., Huang, H., Bennett, B., Snowdon, L., 2012. In: SPE Canadian Unconventional Resources Conference (OnePetro).
Lei, D., Chen, G., Liu, H., Li, X., Tao, K., Cao, J., 2017. Study on the forming conditions and exploration fields of the Mahu giant oil (gas) province, Junggar Basin. Acta Geol. Sin. 91 (7), 1604–1619.
Lei, Q., Weng, D., Xiong, S., Liu, H., Guan, B., Deng, Q., Yan, X., Liang, H., Zeyuan, M.A., 2021. Progress and development directions of shale oil reservoir stimulation technology of China National Petroleum Corporation. Petrol. Explor. Dev. 48 (5), 10.
Li, J., Yin, J., Zhang, Y., Lu, S., Wang, W., Li, J., Chen, F., Meng, Y., 2015. A comparison of experimental methods for describing shale pore features — a case study in the Bohai Bay Basin of eastern China. Int. J. Coal Geol. 152, 39–49.
Li, S., Hu, S., Xie, X., Lv, Q., Huang, X., Ye, J., 2016a. Assessment of shale oil potential using a new free hydrocarbon index. Int. J. Coal Geol. 156, 74–85.
Li, Z., Zou, Y., Xu, X., Sun, J., Li, M., 2016b. Adsorption of mudstone source rock for shale oil–Experiments, model and a case study. Org. Geochem. 92, 55–62.
Li, J., Huang, W., Lu, S., Wang, M., Chen, G., Tian, W., Guo, Z., 2018. Nuclear magnetic ResonanceT1 –t2 map division method for Hydrogen-Bearing components in continental shale. Energy Fuel. 32 (9), 9043–9054.
Li, W., Zhang, Y., Tang, W., 2019. AGU Fall Meeting Abstracts.
Li, J., Jiang, C., Wang, M., Lu, S., Chen, Z., Chen, G., Li, J., Li, Z., Lu, S., 2020a. Adsorbed and free hydrocarbons in unconventional shale reservoir: a new insight from NMR T1-T2 maps. Mar. Petrol. Geol. 116, 104311.
Li, T., Jin, J., Tian, Y., Zhu, R., Liu, Y., 2020b. Chemical characteristics of formation water and the relationship with oil and gas preservation on northwestern margin of Junggar Basin. Petrol. Geol. Exp. 42 (6), 972–980.
Li, W., Cao, J., Zhi, D., Tang, Y., He, W., Wang, T., Xia, L., 2021. Controls on shale oil accumulation in alkaline lacustrine settings: late Paleozoic Fengcheng Formation, northwestern Junggar Basin. Mar. Petrol. Geol. 129, 105107.
Liu, X., Lai, J., Fan, X., Shu, H., Wang, G., Ma, X., Liu, M., Guan, M., Luo, Y., 2020. Insights in the pore structure, fluid mobility and oiliness in oil shales of Paleogene Funing Formation in Subei Basin, China. Mar. Petrol. Geol. 114, 104228.
Liu, Z., Liu, D., Cai, Y., Yao, Y., Pan, Z., Zhou, Y., 2020. Application of nuclear magnetic resonance (NMR) in coalbed methane and shale reservoirs: a review. Int. J. Coal Geol. 218, 103261.
Livo, K., Saidian, M., Prasad, M., 2020. Effect of paramagnetic mineral content and distribution on nuclear magnetic resonance surface relaxivity in organic-rich Niobrara and Haynesville shales. Fuel 269, 117417.
Loucks, R.G., Reed, R.M., Ruppel, S.C., Jarvie, D.M., 2009. Morphology, genesis, and distribution of Nanometer-Scale pores in siliceous mudstones of the mississippian barnett shale. J. Sediment. Res. 79 (12), 848–861.
Meiboom, S., 1958. Modified spin-echo method for measuring nuclear relaxation times. Review of Science Rev. Sci. Instrum. 29.
Michael, E., 2013. Unconventional Resources Technology Conference.
Mukhametdinova, A., Habina-Skrzyniarz, I., Kazak, A., Krzyżak, A., 2021. NMR relaxometry interpretation of source rock liquid saturation — a holistic approach. Mar. Petrol. Geol. 132, 105165.
Müller-Huber, E., Schön, J., Börner, F., 2016. Pore space characterization in carbonate rocks—approach to combine nuclear magnetic resonance and elastic wave velocity measurements. J. Appl. Geophys. 127, 68–81.
Nelson, 2009. Pore-throat sizes in sandstones, tight sandstones, and shales. AAPG Bull. 3 (93), 329–340.
Nicot, B., Vorapalawut, N., Rousseau, B., Madariaga, L.F., Hamon, G., Korb, J., 2016. Estimating saturations in organic shales using 2D NMR. Petrophysics 57 (1), 19–29.
O'Brien, N.R., Cremer, M.D., Canales, D.G., 2002. The Role of Argillaceous Rock Fabric in Primary Migration of Oil.
Piedrahita, J., Aguilera, R., 2017. Estimating oil saturation index OSI from NMR logging and comparison with Rock-Eval pyrolysis measurements in a shale oil reservoir. In: SPE Unconventional Resources Conference.
Qian, M., Jiang, Q., Li, M., Li, Z., Liu, P., Ma, Y., Cao, T., 2017. Quantitative characterization of extractable organic matter in lacustrine shale with different occurrences. Petrol. Geol. Exp. 39 (2), 278–286.
Reed, R.M., Loucks, R.G., 2007. Imaging nanoscale pores in the mississippian barnett shale of the northern Fort Worth Basin. In: AAPG Annual Convention Abstracts.
Romero-Sarmiento, M., Pillot, D., Letort, G., Lamoureux-Var, V., Beaumont, V., Huc, A., Garcia, B., 2016. New Rock-Eval method for characterization of unconventional shale resource systems. Oil Gas Sci. Technol. – Revue d'IFP Energies nouvelles 71 (3), 37.
Rouquerol, J., Avnir, D., Fairbridge, C.W., Everett, D.H., Haynes, J.M., Pernicone, N., Ramsay, J.D., Sing, K.S.W., Unger, K.K., 1994. Recommendations for the characterization of porous solids (Technical Report). Pure Appl. Chem. 66 (8), 1739–1758.
Sang, Q., Zhang, S., Li, Y., Dong, M., Bryant, S., 2018. Determination of organic and inorganic hydrocarbon saturations and effective porosities in shale using vacuum-imbibition method. Int. J. Coal Geol. 200, 123–134.
Siddiqui, M., Ali, S., Fei, H., Roshan, H., 2018. Current understanding of shale wettability: a review on contact angle measurements. Earth Sci. Rev., S444959346
Singer, P.M., 2013. 1D and 2d Nmr Core-Log Integration in Organic Shale.
Sonnenberg, S.A., Pramudito, A., 2009. Petroleum geology of the giant elm coulee field, williston basin. AAPG Bull. 93 (9), 1127–1153.
Tang, Y., Cao, J., He, W., Guo, X., Zhao, K., Li, W., 2021. Discovery of shale oil in alkaline lacustrine basins: the late paleozoic Fengcheng Formation, mahu sag, Junggar Basin, China. Petrol. Sci. 18 (5), 1281–1293.
Van Heek, K.H., 2000. Progress of coal science in the 20th century. Fuel 79 (1), 1–26.
Wang, M., Sherwood, N., Li, Z., Lu, S., Wang, W., Huang, A., Peng, J., Lu, K., 2015. Shale oil occurring between salt intervals in the dongpu depression, Bohai Bay Basin, China. Int. J. Coal Geol. 152, 100–112.
Wang, X., Wang, T., Cao, J., 2018. Basic characteristics and highly efficient hydrocarbon generation of alkaline? Lacustrine source rocks in fengcheng formation of mahu sag. Xinjing Pet. Geol. 39 (1), 1.
Wang, S., Feng, Q., Zha, M., Lu, S., Qin, Y., Xia, T., Zhang, C., 2015. Molecular dynamics simulation of liquid alkane occurrence state in pores and slits of shale organic matter. Petrol. Explor. Dev. 42 (6), 844–851.
Wang, M., Ma, R., Li, J., Lu, S., Li, C., Guo, Z., Li, Z., 2019. Occurrence mechanism of lacustrine shale oil in the paleogene Shahejie Formation of jiyang depression, Bohai Bay Basin, China. Petrol. Explor. Dev. 46 (4), 833–846.

Wang, S., Wang, G., Huang, L., Song, L., Huang, Y., 2021. Logging evaluation of lamina structure and reservoir quality in shale oil reservoir of Fengcheng Formation in Mahu Sag, China. Mar. Petrol. Geol. (3), 105299

Washburn, K.E., Birdwell, J.E., 2013. Updated methodology for nuclear magnetic resonance characterization of shales. J. Magn. Reson. 233, 17–28.

Xia, L., Cao, J., Stüeken, E.E., Zhi, D., Wang, T., Li, W., 2020. Unsynchronized evolution of salinity and pH of a Permian alkaline lake influenced by hydrothermal fluids: a multi-proxy geochemical study. Chem. Geol. 541, 119581.

Yao, Y., Liu, D., Che, Y., Tang, D., Tang, S., Huang, W., 2010. Petrophysical characterization of coals by low-field nuclear magnetic resonance (NMR). Fuel 89 (7), 1371–1380.

Yu, K., Cao, Y., Qiu, L., 2019. Resource potentials of soda and boron in the lower permian fengcheng formation of the mahu sag in northwestern junggar basin, China. Acta Geologica Sinica - English Edition 93 (2), 483–484.

Zhang, Z., Yuan, X., Wang, M., Zhou, C., Tang, Y., Chen, X., Lin, M., Cheng, D., 2018. Alkaline-lacustrine deposition and paleoenvironmental evolution in permian Fengcheng Formation at the mahu sag, Junggar Basin, NW China. Petrol. Explor. Dev. 45 (6), 1036–1049.

Zhang, P., Lu, S., Li, J., 2019. Characterization of pore size distributions of shale oil reservoirs; A case study from Dongying Sag, Bohai Bay Basin, China. Mar. Petrol. Geol. 100, 297–308.

Yu, K, Cao, Y, Qiu, L, Sun, P, 2019. Depositional environments in an arid, closed basin and their implications for oil and gas exploration: The lower Permian Fengcheng Formation in the Junggar Basin, China. Aapg Bull 103 (9), 2073–2115.

Zhang, H., Huang, H., Li, Z., Liu, M., 2020. Comparative study between sequential solvent-extraction and multiple isothermal stages pyrolysis: a case study on Eocene Shahejie Formation shales, Dongying Depression, East China. Fuel 263, 116591.

Zhang, P., Lu, S., Li, J., Chang, X., Lin, Z., Chen, G., Li, J., Liu, J., Tian, S., 2022. Evaluating microdistribution of adsorbed and free oil in a lacustrine shale using nuclear magnetic resonance: a theoretical and experimental study. J. Petrol. Sci. Eng. 212, 110208.

Zheng, M., Fan, X., He, W., Yang, T., Tang, Y., Ding, J., Wu, H., Chen, L., Guo, J., 2019. Superposition of deep geological structural evolution and hydrocarbon accumulation in the Junggar Basin. Earth Sci. Front. 26 (1), 22.

Zhi, D., Cao, J., Xiang, B., Qin, Z., Wang, T., 2016. Fengcheng alkaline lacustrine source rocks of Lower Permian in Mahu Sag in Junggar Basin: hydrocarbon generation mechanism and petroleum resources reestimation. Xinjing Pet. Geol. 37 (5), 1.

Zhi, D., Tang, Y., He, W., Guo, X., Zheng, M., Huang, L., 2021. Orderly coexistence and accumulation models of conventional and unconventional hydrocarbons in lower permian Fengcheng Formation, mahu sag, Junggar Basin. Petrol. Explor. Dev. 48 (1), 43–59.

Zhu, C., Guo, W., Li, Y., Gong, H., Sheng, J.J., Dong, M., 2021. Effect of occurrence states of fluid and pore structures on shale oil movability. Fuel 288, 119847.

Zou, C., Zhu, R., Chen, Z., Ogg, J.G., Wu, S., Dong, D., Qiu, Z., Wang, Y., Wang, L., Lin, S., et al., 2019. Organic-matter-rich shales of China. Earth Sci. Rev. 189, 51–78.

Lewis, R., Singer, P., Jiang, T., Rylander, E., & Mclin, R. H., 2013. NMR T2 Distributions in the Eagle Ford Shale: Reflections on Pore Size.